

RESEARCH ARTICLE | AUGUST 13 2024

## Effects of entry angle on the water-entry cavity and motion hydrodynamics of a hollow cylinder

Zhengui Huang (黄振贵) ; Yu Hou (侯宇)  ; Xiaowei Cai (蔡晓伟); Zhihua Chen (陈志华); Yiming Xu (徐一鸣); Jian Qin (秦健)



*Physics of Fluids* 36, 082107 (2024)

<https://doi.org/10.1063/5.0220325>



View  
Online



Export  
Citation



Physics of Fluids

Special Topic:

Kitchen Flows 2024

Guest Editors: Gerald G. Fuller, Maciej Lisicki, Arnold J.T.M. Mathijssen, Endre Joachim Mossige, Rossana Pesquino, Vivek Nagendra Prakash, Laurence Ramos

[Submit Today!](#)

# Effects of entry angle on the water-entry cavity and motion hydrodynamics of a hollow cylinder

Cite as: Phys. Fluids **36**, 082107 (2024); doi: [10.1063/5.0220325](https://doi.org/10.1063/5.0220325)

Submitted: 24 May 2024 · Accepted: 24 July 2024 ·

Published Online: 13 August 2024





View Online



Export Citation



CrossMark

Zhengui Huang (黄振贵),<sup>1</sup>  Yu Hou (侯宇),<sup>2,a)</sup>  Xiaowei Cai (蔡晓伟),<sup>3</sup> Zhihua Chen (陈志华),<sup>1</sup> Yiming Xu (徐一鸣),<sup>2</sup> and Jian Qin (秦健)<sup>1</sup>

## AFFILIATIONS

<sup>1</sup>National Key Laboratory of Transient Physics, Nanjing University of Science and Technology, Nanjing 210094, China

<sup>2</sup>School of Electrical Engineering and Automation, Nantong University, Nantong 226019, China

<sup>3</sup>National Key Laboratory of Hydrodynamics, China Ship Scientific Research Center, Wuxi 214082, China

<sup>a)</sup> Author to whom correspondence should be addressed: [houyu@ntu.edu.cn](mailto:houyu@ntu.edu.cn)

## ABSTRACT

The oblique water entry of a hollow cylinder at various entry angles is numerically studied. The formation characteristics of the internal and external cavities, the curling splash, and the underwater rotation of the cylinder are revealed and analyzed. Our results show that asymmetric left- and right-attached cavities form near both the inner and outer walls of the cylinder. There are different formation patterns for the internal cavity between the left and right sides. The left internal cavity is mainly formed by the cavity shrinkage after closure, whereas the right internal cavity is formed by internal flow separation at small water-entry angles. An inclined concavity forms on the through-hole jet tip, induced by the rightward-curling splash. The rotation direction of the cylinder varies with entry angles and a critical angle exists. A periodic hydrodynamic force and moment are observed as the cylinder swings from side to side, resulting in a steady tail-slap motion.

Published under an exclusive license by AIP Publishing. <https://doi.org/10.1063/5.0220325>

## I. INTRODUCTION

The entry of moving objects into water induces complex multi-phase flow phenomena,<sup>1</sup> including cavity evolution, jet formation, and a curling splash. Structural deformation,<sup>2–4</sup> trajectory deflection, and even body bouncing<sup>5</sup> and destruction may occur under the tremendous impact and nonlinear hydrodynamic forces. Extensive investigations on these water-entry issues have great significance in nature,<sup>6,7</sup> diving sports,<sup>8</sup> seaplane landing,<sup>9</sup> ship slamming,<sup>10</sup> and military fields such as aerial torpedoes<sup>11</sup> and trans-media projectiles.<sup>1,12,13</sup> Therefore, the fundamental physical mechanisms concerning slam loads, cavities, and motion instability continue to be studied.

Several specific simplified objects were investigated in early water-entry investigations. Solid rigid spheres were widely studied in initial work on the effects of the water-entry conditions<sup>14,15</sup> (velocity and angle) and surface conditions<sup>16–18</sup> (hydrophilic or hydrophobic) on the impact force and cavity dynamics. Moreover, the initial spinning,<sup>17,19</sup> the launching mode,<sup>20,21</sup> and sphere dimensions have been deeply studied in terms of their effects on the air-entraining cavity evolution. With practical applications in ship slamming, bullet penetration, and drag-reduction cavitation, other simplified solid structures have been investigated, including wedges,<sup>10</sup> disks,<sup>22,23</sup> cones,<sup>24</sup> and slender cylinders with various nose shapes.<sup>25,26</sup> Their water-entry

cavity dynamics and motion hydrodynamics have been further investigated with different geometrical structures, shapes, and dimensions.

In-depth investigations on the water entry of solid objects have been carried out under more realistic fluid-structure interactions with a rotating liquid,<sup>27</sup> flowing stream,<sup>28</sup> waves,<sup>12</sup> and floating ice.<sup>29,30</sup> The objects entering the water have also evolved into more intricate structures, featuring local protrusions,<sup>31</sup> deep holes,<sup>2,32,33</sup> through holes,<sup>34–38</sup> dimples,<sup>39</sup> and other elements. Some interesting phenomena have been found in these water-entry processes, such as trajectory deflection, cavity fluctuation, internal jets, and trapped air. Further investigations are warranted for improving trans-media vehicles, projectiles, and aircraft.

Recent investigations have examined the water entry of a structure with a through-hole. Early investigations focused on the vertical water entry of a horizontal cylinder shell. A two-dimensional boundary element method was used by Sun and Faltinsen<sup>40</sup> to simulate the water impact of horizontal cylindrical shells, and the effects of the additional mass, initial water entry velocity, and force on the calculated natural frequencies were discussed. The water entry of a horizontal hollow cylinder was studied by Lyu *et al.*,<sup>41</sup> and they showed that cylinder trajectories collapse in the initial immersion stage when the velocity ratios are the same. The overall shell deformation of flexible thin cylinders

was studied by Panciroli *et al.*<sup>4</sup> in the case of water entry and found to follow the first mode shape of vibration of a free ring, while the stresses were observed to be influenced by the superposition of the higher mode shapes induced by the impact.

The water entry of upright hollow cylinders was initially investigated by Hou *et al.*<sup>38</sup> for designing a trans-media hollow projectile. Hollow projectiles enable greater penetration and are subject to less fluid drag than typical solid structures. They also have a positive potency in future underwater defense because the cavity flow induced by hollow disks with  $D_{\text{hole}}/D=0.6$  has a relatively low drag coefficient.<sup>42</sup> However, the detailed physical mechanisms remain unclear due to several new phenomena induced by the through-hole during water entry, including a trapped bubble on the jet tip, a ringlike tail cavity, and both external and internal cavities. The vertical water entry of hollow cylinders has been further investigated by Hou *et al.*<sup>43</sup> and Zhou *et al.*,<sup>36</sup> who reported that the cavity closure pattern changes with the increasing water-entry velocity and inner cylinder diameters. Moreover, effects of different hole shapes on the vertical water-entry process were experimentally studied by Jafari and Akbarzadeh.<sup>34</sup> The highest through-hole jet and the greatest resistance to cavity sealing were found in a cylinder with a downward conical hole under the same water-entry conditions. The high-speed vertical water entry of hollow projectiles with different aperture sizes and velocities has also been numerically studied by Fan *et al.*<sup>44</sup> They showed that the friction resistance increases with the increasing velocity and the decreasing aperture ratio.

Considering the random waves<sup>9,12,45</sup> and ripples that appear on the water surface, most projectiles enter the water at a certain angle between the projectile axis and the free surface. An asymmetric force will be formed, leading to cavity collapse, trajectory instability, and attitude rotation. The oblique water entry of hollow cylinders has been investigated experimentally by Hou *et al.*<sup>35</sup> and Liu *et al.*<sup>46</sup> They discussed the evolution and flow mechanism of cavities, jets, and splashes at various inclined water-entry velocities and inner diameters. However, the opaque materials used in their experiments limited the observation of the formation of internal cavities and jets, especially regarding the physical mechanism of cavities on both sides of the object and the curling jet. Moreover, the effects of the water-entry angle on the internal multiphase flow have not yet been elucidated, despite their great significance for the dynamics of hollow projectiles. Numerical investigations on the oblique water entry of hollow cylinders could reveal the internal flow field and cylinder motion parameters. Therefore, this paper investigates the oblique water entry of hollow cylinders in three-dimensional (3D) numerical simulations. The focus is studying the effects of the water-entry angle on the multiphase flow and motion hydrodynamics.

This remainder of this paper is organized as follows. Section II describes the numerical method, including the governing equations, turbulence model, boundary conditions and mesh generation. Section III mainly presents and analyzes the results. Section III A discusses the validation of the numerical model, Sec. III B highlights the disparities in the multiphase flow and motion hydrodynamics between the vertical and oblique water entry of a hollow cylinder, and Sec. III C analyzes the effects of the water-entry angle on the cavity evolution, jet formation, cylinder rotation, and hydrodynamic force. Finally, the main findings are summarized in Sec. IV.

## II. NUMERICAL METHOD

### A. Governing equations and turbulence model

A constant room temperature and an incompressible turbulent flow hypothesis are considered. Governing equations are based on volume of fluid (VOF) multiphase model, which includes the following mass and momentum conservation equations.

Mass conservation equation

$$\frac{\partial \rho_m}{\partial t} + \frac{\partial(\rho_m u_j)}{\partial x_j} = 0, \quad (1)$$

where  $\rho_m = (1 - \beta_w)\rho_a + \beta_w \rho_w$  is the mixture density.  $\rho_a$  and  $\rho_w$  are the density of air and water, respectively.

Momentum conservation equation

$$\frac{\partial \rho_m u_i}{\partial t} + \frac{\partial(\rho_m u_i u_j)}{\partial x_j} = \rho_m g_i - \frac{\partial P}{\partial x_i} + \frac{\partial}{\partial x_j} \left[ (\mu_m + \mu_t) \left( \frac{\partial u_i}{\partial x_j} + \frac{\partial u_j}{\partial x_i} \right) \right], \quad (2)$$

where  $P$  and  $g_i$  are the pressure and the gravitational acceleration component in the Cartesian coordinate system, respectively;  $\mu_m = (1 - \beta_w)\mu_a + \beta_w \mu_w$  denotes the mixture dynamic viscosity coefficient and  $\mu_t$  is the turbulent viscosity.

The Realizable  $k$ - $\epsilon$  turbulence model proposed by Shih *et al.*<sup>47</sup> is used to close the viscous equations. The turbulent kinetic transport equation ( $k$ ) is given as

$$\begin{aligned} \frac{\partial(\rho_m k)}{\partial t} + \frac{\partial(\rho_m k u_i)}{\partial x_i} &= \frac{\partial}{\partial x_i} \left[ \left( \mu + \frac{\mu_t}{\sigma_k} \right) \frac{\partial k}{\partial x_i} \right] + G_k + G_b - \rho_m \epsilon \\ &\quad - Y_M + S_k. \end{aligned} \quad (3)$$

The transport equation of the dissipation rate of energy in the turbulent flow ( $\epsilon$ ) is written as

$$\begin{aligned} \frac{\partial(\rho_m \epsilon)}{\partial t} + \frac{\partial(\rho_m \epsilon u_i)}{\partial x_i} &= \frac{\partial}{\partial x_i} \left[ \left( \mu + \frac{\mu_t}{\sigma_\epsilon} \right) \frac{\partial \epsilon}{\partial x_i} \right] + \rho C_1 S \epsilon \\ &\quad - \rho C_2 \frac{\epsilon^2}{k + \sqrt{\nu \epsilon}} + C_{1\epsilon} \frac{\epsilon}{k} C_{3\epsilon} G_b + S_\epsilon, \end{aligned} \quad (4)$$

where  $C_1 = \max[0.43, \frac{\eta}{\eta+5}]$ ,  $\eta = S \frac{k}{\epsilon}$ , and  $S = \sqrt{2S_{ij}S_{ij}}$ .

In these equations,  $G_k = \mu_t S^2$  and  $G_b = \beta g_i \frac{\mu_t}{Pr_t} \frac{\partial T}{\partial x_i}$  represent the generation of turbulent kinetic energy due to the mean velocity gradients and buoyancy, respectively. The default value of  $Pr_t$  is 0.85 and  $\beta = -\frac{1}{\rho} \left( \frac{\partial \rho}{\partial T} \right)_p$ .  $Y_M = 2\rho k \epsilon / \gamma RT$  represents the contribution of the fluctuating dilatation incompressible turbulence to the overall dissipation rate.  $C_2$  and  $C_{1\epsilon}$  are constants.  $\sigma_k$  and  $\sigma_\epsilon$  are the turbulent Prandtl numbers of  $k$  and  $\epsilon$ , respectively. In this work,  $C_2 = 1.9$ ,  $C_{1\epsilon} = 1.44$ ,  $\sigma_k = 1.0$ , and  $\sigma_\epsilon = 1.2$  are used as the default values. No extra source terms for  $S_k$  and  $S_\epsilon$  are defined.

In this numerical simulation, finite volume method (FVM) is used to discretely solve the above time-dependent governing equations, the SIMPLE scheme is used to solve the pressure-velocity coupling algorithms, and the PRESTO scheme is used for pressure interpolation. The convection term uses a second-order upwind discretization equation, the diffusion term uses a second-order central difference discretization format, the transient term uses a first-order implicit

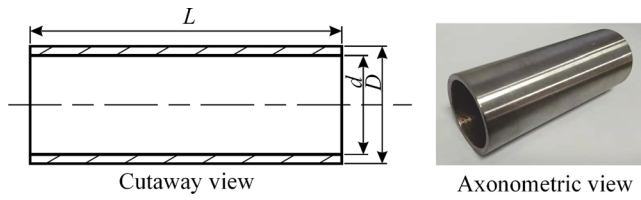


FIG. 1. Schematic of the water-entry cylinder.

discretization, and the gradient term is based on the least squares cell-based interpolation equation. The Geo-Reconstruct scheme is employed for solving the transport equation for the volume fractions.

**B. Boundary conditions and mesh generation**

In this work, the hollow cylinder is the same as the model M1 used by Hou *et al.*,<sup>35</sup> as shown in Fig. 1. It is made of ASTM1045 steel and its geometric parameters are listed in Table I. The characteristic length is  $D_c = (D^2 - d^2)^{1/2} = 16.1$  mm. The Froude number  $Fr = v_0 / (g D_c)^{1/2} = 7-8$ , Bond number  $B_0 = \rho g D_c^2 / \gamma \gg 1$ , and Weber number  $We = \rho v_0^2 D_c / \gamma = 1800-2200$ , where  $v_0$  is the entry velocity of the cylinder,  $\rho = 998.2$  kg·m<sup>-3</sup> is the density of water, and  $\gamma$  denotes the surface tension.

The geometrical dimensions of the computational domain with a water depth of  $17D$  are  $18D \times 12D \times 23D$ , as shown in Fig. 2. The upper boundary is set as a pressure inlet, while the remaining boundaries are defined as solid walls. The coordinate systems for time and space are consistent with those used by Hou *et al.*,<sup>35</sup> where the spatial origin ( $o$ ) is defined as the intersection between the hollow cylinder axis and water surface, and the time origin is set at the moment when the projectile passes through point  $o$ . The  $x$ -axis represents the direction of gravity, the  $y$ -axis denotes the horizontal direction, and the  $z$ -axis indicates the lateral direction.

The overset mesh technique combined with 6-degrees-of-freedom motion is used to capture the moving projectile. An overset mesh is generated for the computational domain (Fig. 3), including a component mesh and a background mesh. Figure 3(d) shows the combined mesh distribution after all preprocessing steps, such as hole-cutting. The entire computational domain is divided by cut-cell meshes. The areas near the free surface, the motion trajectory, and the geometric wall are further refined to capture flow phenomena such as the splash, cavity evolution, and internal jets.

Five mesh resolutions for the computational domain, covering coarser ( $1.55 \times 10^6$  grid cells), coarse ( $2.13 \times 10^6$ ), medium ( $2.46 \times 10^6$ ), fine ( $3.32 \times 10^6$ ), and finer ( $4.68 \times 10^6$ ) grids, are examined to ensure that the results are independent of the mesh used for the simulations. The projectile displacements under these five mesh resolutions are compared in Fig. 4. The motion parameters given by the different grid resolutions are similar, with only minor numerical discrepancies. Considering both accuracy and computational efficiency, the medium

TABLE I. Details of the hollow cylinder.

$D/\text{mm}$	$d/\text{mm}$	$d/D$	$L/\text{mm}$	$M/\text{kg}$	$\rho_s/\text{kg}\cdot\text{m}^3$
30.0	25.3	0.84	80.0	0.128	7850

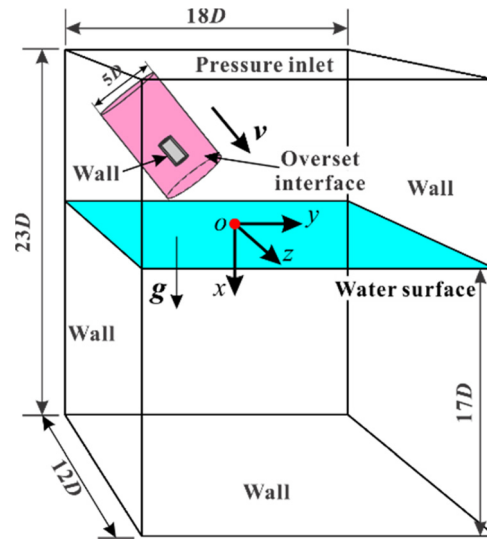


FIG. 2. Diagram of computational domain and boundary conditions.

mesh of 2.46 million cells is selected for subsequent numerical simulations of the oblique water entry of the hollow cylinder.

**III. RESULTS AND DISCUSSION**

**A. Validation of the numerical model**

To validate the accuracy of the numerical model for simulating the water-entry cavity evolution, the oblique water entry of model M1 in Hou *et al.*<sup>35</sup> is simulated with the selected mesh generation. The same operating conditions are set as the referenced experiments<sup>35</sup> including an initial water-entry angle of  $\alpha_w = 60^\circ$  and a water-entry velocity of  $v_0 = 2.93$  m/s. The comparison of the oblique water-entry cavity evolution between the experimental and numerical results is shown in Fig. 5. Several typical flow phenomena in the experiment, such as the open right cavity and splash, the bending of the through-hole jet, and the left cavity closure, are clearly captured by the simulation. This indicates that the numerical model in this paper can predict the cavity evolution effectively in the oblique water-entry of a hollow cylinder.

The time origin ( $t = 0$  ms) is set at the moment when the center of cylinder head reaches the water surface. The spatial origin ( $o$ ) is defined as the intersection between the hollow cylinder axis and water surface at  $t = 0$  ms, as shown in Fig. 5, where  $x, y, z = 0$  mm. The  $x$ -axis represents the direction of gravity, the  $y$ -axis denotes the horizontal direction, and the  $z$ -axis indicates the lateral direction. The projectile displacements and velocities along  $x$  and  $y$  axis in the experimental and numerical results are compared in Fig. 6. The variations of both displacements and velocities along  $x$  and  $y$  axis are in good agreement with the experimental data, with a maximum error of about 5.2% in displacement and 9.5% in velocity. It indicates that the numerical model correctly predicts the oblique water-entry motion of the hollow cylinder. Considering the absence of any initial lateral ( $z$ ) velocity in the projectile and because the model experiences nearly symmetric forces on both sides upon immersion, the displacement in the  $z$ -axis direction remains relatively small ( $z \leq 0.66$  mm). Thus, this paper

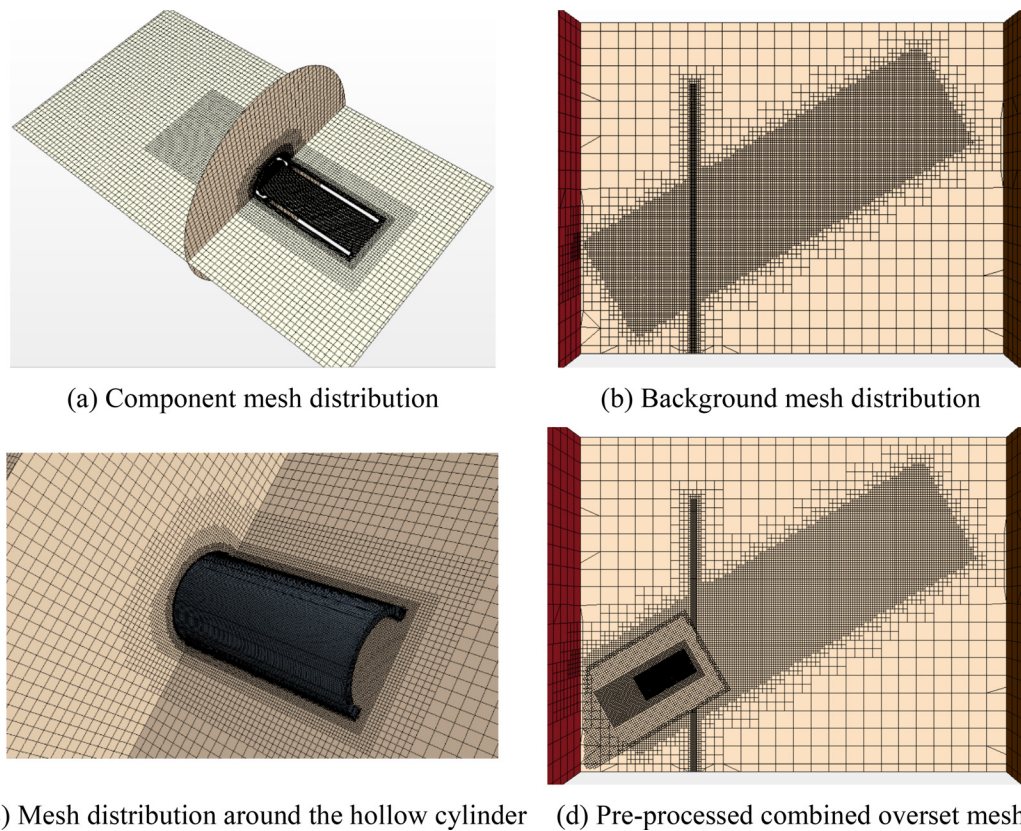


FIG. 3. Overset mesh generation for the computational domain.

focuses on the translational motion of the projectile along the vertical ( $x$ ) and horizontal ( $y$ ) directions, and the rotation around the  $z$ -axis.

Furthermore, to verify the accuracy of flow field, the vertical water-entry case ( $\alpha_w = 90^\circ$ ) of hollow cylinder is also solved in Fig. 7 as a validated example using this work's numerical model. The cavity evolution and pressure contours are shown in Figs. 7(a) and 7(b) respectively. The typical internal flow phenomena can be captured well in the simulation, including the top bubble, through-hole jet, internal

cavity, and shedding bubbles, which are in good agreement with the experimental and numerical data in Hou *et al.*<sup>38</sup> and Hou *et al.*<sup>43</sup> The pressure contours of the flow field are consistent with the pressure characteristics of hollow cylinders, including high pressure induced by impact, low pressure in the internal cavity and pressure fluctuation near the inside wall. In a word, the numerical method can be applicable to simulate the water entry of hollow cylinder at different entry angles.

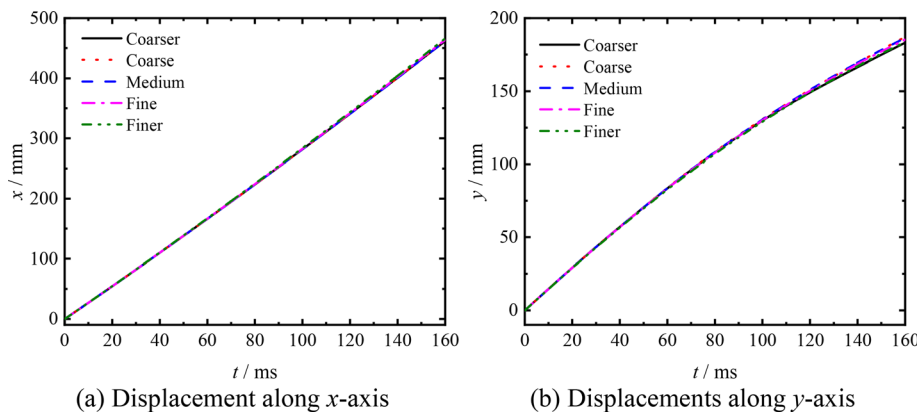


FIG. 4. Comparison of the projectile displacement using five mesh resolutions.

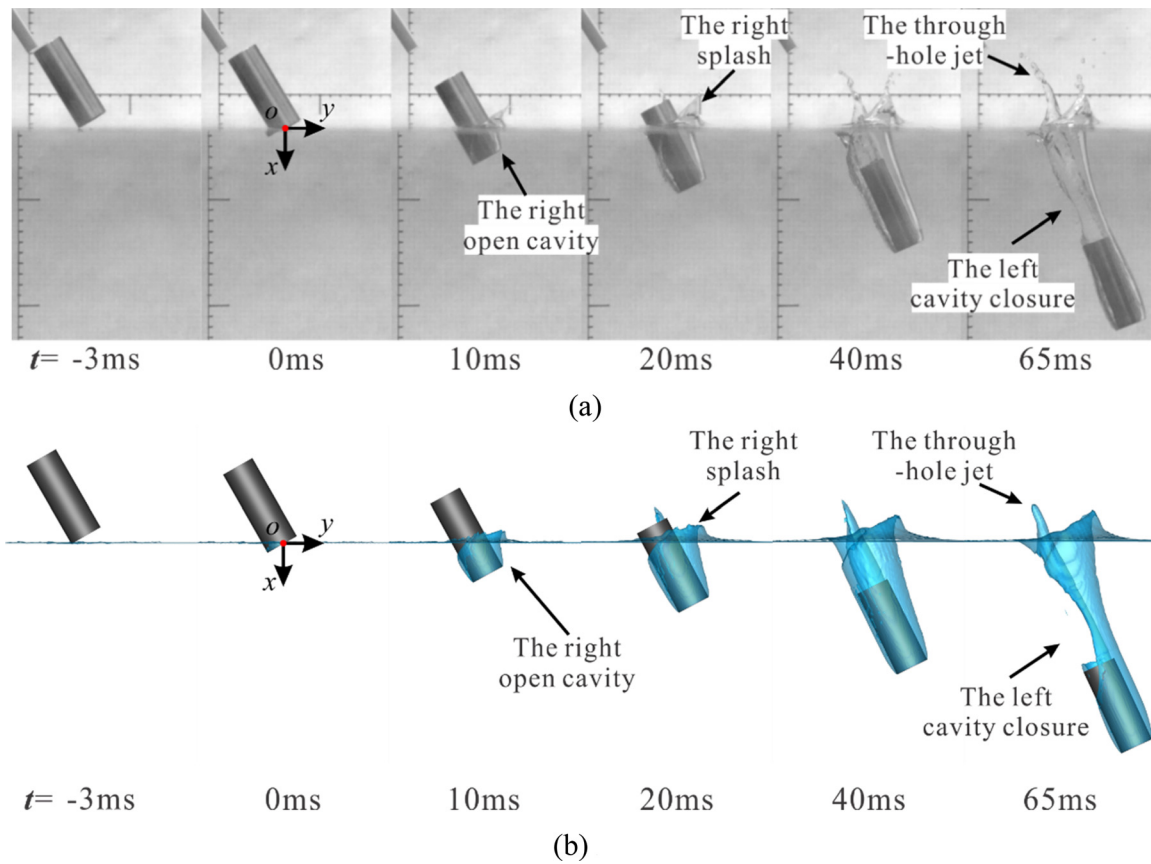


FIG. 5. Comparison of oblique water-entry cavity evolution between (a) experimental and (b) numerical results.

**B. Disparities between vertical and oblique water entry of a hollow cylinder**

The vertical water entry ( $\alpha_w = 90^\circ$ ) of hollow cylinder M1 is first studied using 3D simulations based on our numerical model. Figure 7 shows the key phenomena observed during the cavity evolution, including the formation of a top bubble, ejection of a through-hole jet, surface closure, and deep closure. Both the internal and external multiphase flows exhibit approximately symmetric patterns

during their evolution. Further details on the hydrodynamic mechanism can be found in Hou *et al.*<sup>43</sup> However, most projectiles enter the water at a smaller entry angle than this extreme case. To study the hydrodynamic disparities between vertical and oblique water entry, we first analyze the water entry of M1 at an entry angle of  $\alpha_w = 60^\circ$  and an entry velocity of  $v_0 = 2.93$  m/s. The characteristics of the multiphase flow and motion hydrodynamics are presented in the following subsections.

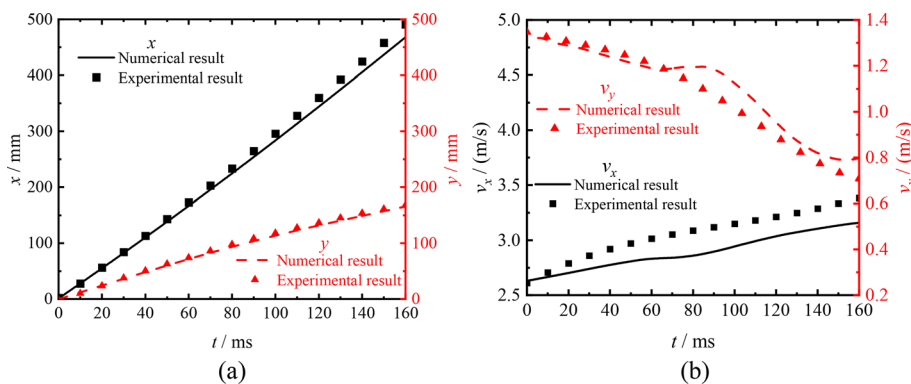


FIG. 6. Comparison of the projectile (a) displacements and (b) velocities along x and y axis between experimental and numerical results in the oblique water entry.

20 August 2024 01:09:19

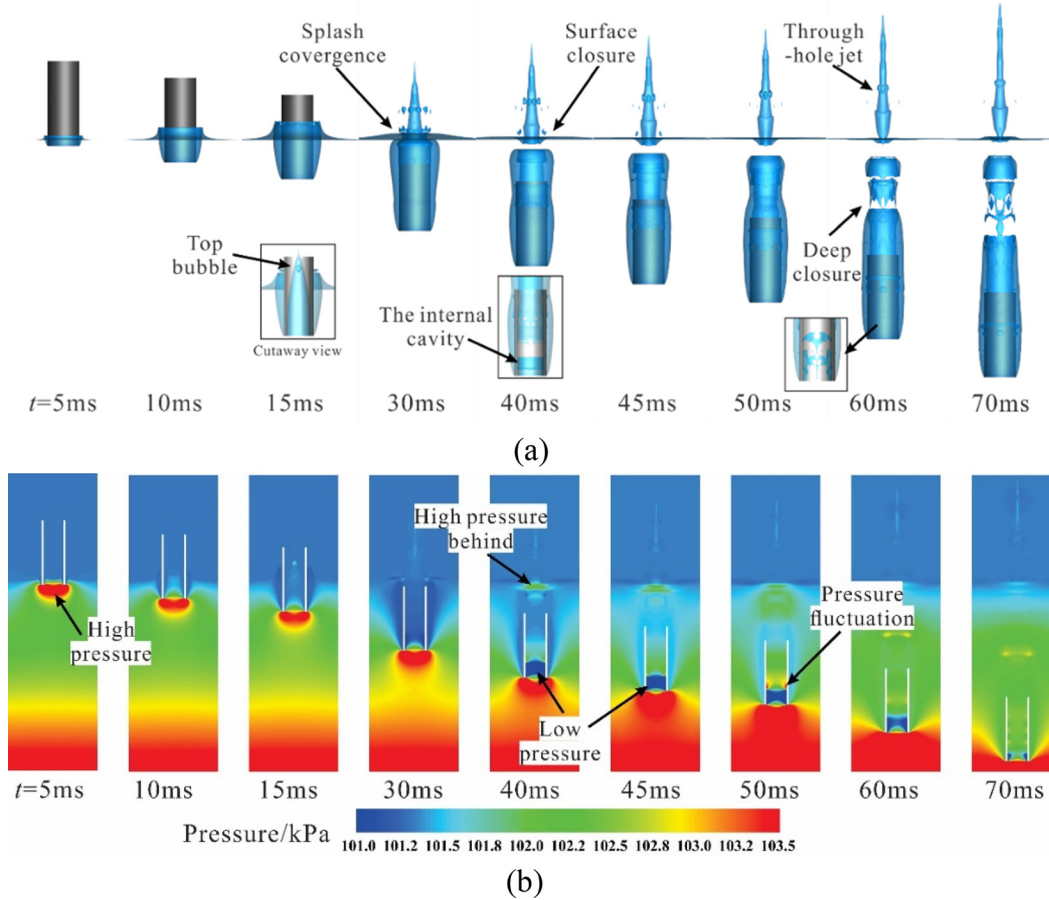


FIG. 7. (a) Cavity evolution and (b) pressure contours in the vertical water entry of hollow cylinder ( $\alpha_w = 90^\circ$ ).

1. Cavity evolution and jet formation

a. External cavity. The external cavity evolution of a hollow cylinder entering water at  $\alpha_w = 60^\circ$  within the period  $t = 0 - 130$  ms is shown in Figs. 8 and 9. The impact and open cavity stages occur from  $t = 0 - 50$  ms, followed by the cavity closure from  $t = 50 - 80$  ms. Subsequently, underwater motion with an attached cavity persists for  $t > 80$  ms. Remarkably, the simulation reveals more discernible variations in the cavity structure than the experimental observations.

During the impact stage, the left cylinder head initially hits the water surface with an inclined body at  $t = -3$  ms. The nearby fluid

particles acquire kinetic energy and splash outward upon the impact, leading to cavity expansion. The extent of the cavity expansion varies depending on the respective flow regions. The outer area around the left cylinder head is located in a backflow region, where the fluid particles acquire less velocity normal to the sidewall and encounter greater resistance when expanding in the lower-left direction. Therefore, a smaller open cavity forms in this particular region. Limitations to the experimental conditions mean that Fig. 5(a)<sup>35</sup> does not clearly depict this tiny cavity from  $t = 0 - 5$  ms. However, an initial distinct cavity structure appears around both the front and rear sides of the cylinder

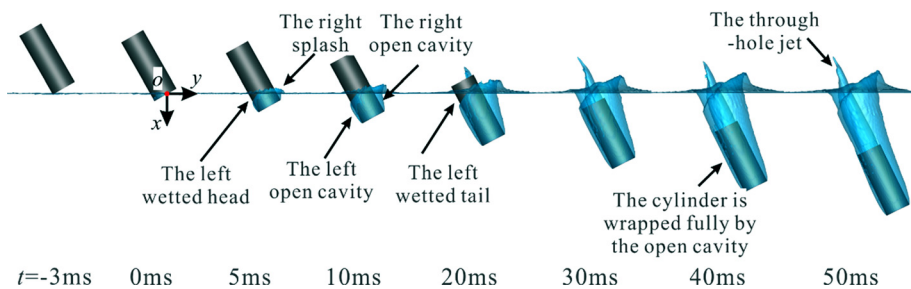


FIG. 8. Cavity evolution of oblique water entry from  $t = -3 - 50$  ms ( $\alpha_w = 60^\circ$ ).

20 August 2024 01:09:19

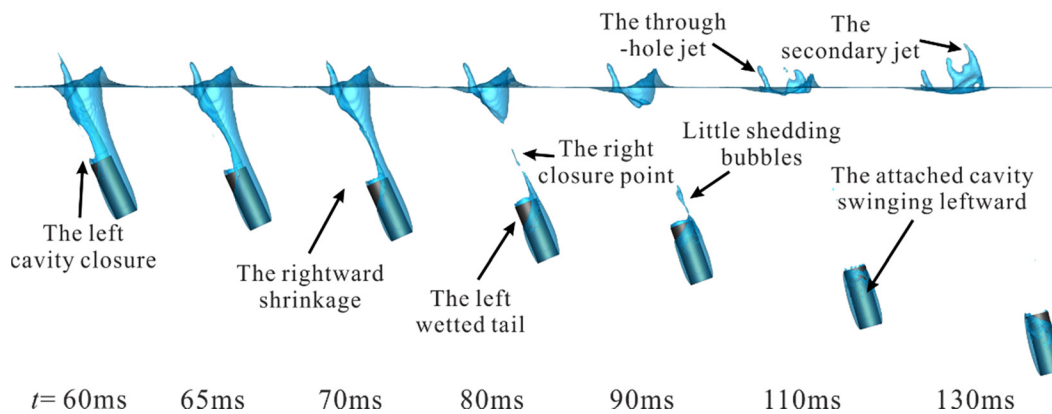


FIG. 9. Cavity evolution of the oblique water entry at  $t = 60\text{--}130\text{ ms}$  ( $\alpha_w = 60^\circ$ ).

head at  $t = 0\text{ ms}$  in Fig. 8. This structure gradually expands toward the right as the solid-liquid contact point moves along the water surface. Unfortunately, the experiment<sup>35</sup> did not capture this specific cavity formation due to its forward-shooting perspective.

The specific cavity gradually expands until the right cylinder head reaches the water surface, as shown in Fig. 8 for  $t = 5\text{--}10\text{ ms}$ . The fluid particles around the right incident flow region acquire more kinetic energy from the projectile extrusion, and thus generate a more visible splash and open cavity over the water surface. On the left side of the cylinder, where a smaller open cavity has formed, there is a certain degree of wetting as the projectile enters the water (Fig. 8 at  $t = 20\text{ ms}$ ). As the surrounding cavity expands and its volume increases, the projectile eventually becomes fully wrapped by the open cavity once  $t > 30\text{ ms}$ . Shortly thereafter, the left cavity begins to shrink, with the cavity expansion stage ending at  $t = 50\text{ ms}$ .

During cavity closure, the left cavity wall first touches the internal jet at  $t \approx 58\text{ ms}$  and starts to pinch off (Fig. 9). The closure point gradually moves rightward along the jet column until the right cavity wall pinches off on the jet at  $t = 80\text{ ms}$ . Because the left cavity pinches off and shrinks downwards prematurely, the left cavity wall passes through the cylinder tail earlier than the right cavity wall. The left cylinder tail becomes wetted before the right side. Tail slapping occurs on the left and produces a hydrodynamic force to the right acting on the cylinder tail, which causes the cylinder to rotate clockwise. After the right cavity closure, small shedding bubbles appear behind the attached cavity. These are generated by the intermittent contact between the shrinking cavity and the internal jet. As the right cavity wall shrinks to the cylinder tail, the attached cavity will deviate to the left as the cylinder rotates clockwise. Hence, the left cylinder tail enters the cavity while the right cylinder tail becomes wetted at  $t = 130\text{ ms}$ . These repeated wetting processes lead to multiple occurrences of the tail-slapping phenomenon.

*b. Through-hole jet.* To further investigate the evolution characteristics of the through-hole jet during oblique water entry, Fig. 10 shows the formation and evolution of the through-hole jet from  $t = -3\text{--}30\text{ ms}$  during the impact and open cavity stages. The air-liquid flow is illustrated on the vertical symmetry plane of the projectile, namely, the  $oxy$  plane.

The internal jet forms at  $t = -3\text{ ms}$  when the bottom-left side of the cylinder hits the water in Fig. 10(a). When the cylinder bottom impacts the water, the surrounding flow is compressed and sprays toward both sides of the through-hole. The left side of the inner wall is located in the incident flow region, where the fluid particles experience enhanced kinetic energy due to the frontal impact. The liquid ejection normal to the left sidewall is more visible and produces a continuous splash toward the upper-right at  $t = 0\text{ ms}$ . In contrast, the fluid particles near the outer side of the left wall move along the projectile wall in the axial direction, with little vertical movement. The left outer wall remains wetted after entering the water and the left open cavity does not form until  $t = 2\text{--}4\text{ ms}$  in Figs. 10(c) and 10(d).

The shape of the upper surface of the left splash becomes concave inward toward the right, because the left jet initially moves toward the upper-right region. The internal jet rolls toward the right overall, as shown in Fig. 10(d). The right inner wall of the hole remains wetted in the backflow region after the immersion of the right cylinder head at  $t = 2\text{ ms}$ . Unlike the symmetric concave shape of the through-hole jet tip in the case of vertical water entry (Fig. 7), there is no obvious splash and the jet tip forms a single-sided concavity. Furthermore, no top bubble forms on the top of the internal jet during oblique water entry. As the jet tip rolls and reaches the other sidewall, a distinct cavity forms on top of the internal jet in the  $oxy$  plane [Fig. 10(g)]. This cavity gradually shrinks under the extrusion from the rising jet and right sidewall as the internal jet moves upwards along with the right inner wall. Under the guidance of the right inner wall, the direction in which the internal jet is ejected changes from upper-right to upper-left upon exiting from the through-hole. The through-hole jet then gradually bends under gravity in Fig. 10(k). Overall, these numerical flow details explain the change in ejection direction observed in the experiment.<sup>35</sup>

The pressure contours around the vertical symmetry plane of the hollow cylinder at the moment of impact are shown in Fig. 11. The impact forms a high-pressure flow region on the bottom inner wall of the projectile in Fig. 11(a). A pressure gradient toward the upper-right can be observed at  $t = 0\text{ ms}$ . This significant pressure difference induces the upper-right movement of the fluid and generates the splash near the left inner wall. The high-pressure region is mainly located near the inner wall and has relatively little influence on the external fluid due to isolation by the sidewall. Thus, no obvious open cavity



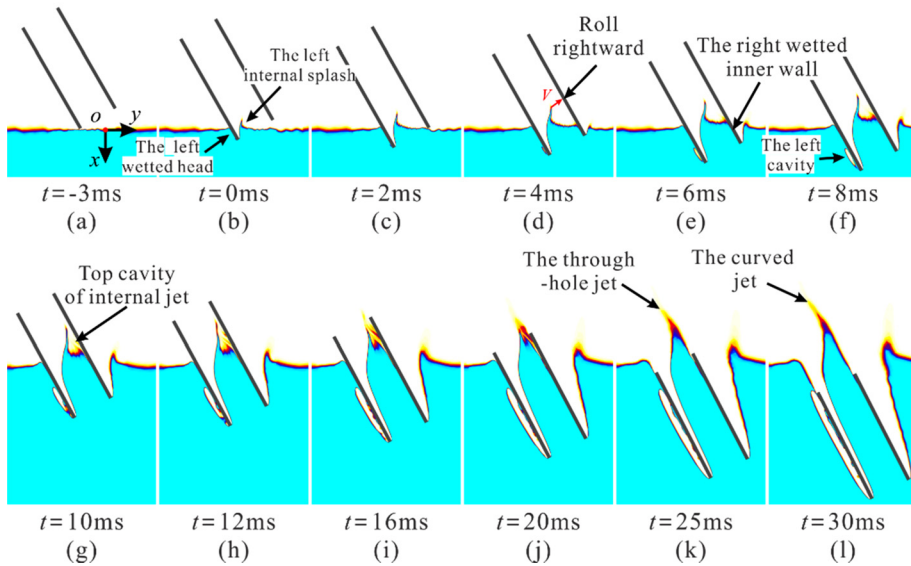


FIG. 10. Evolution of the through-hole jet during oblique water entry in oxy plane.

initially forms on the outer side of the left wall. Similarly, a splash only occurs on the outer side of the right wall, while its inner side remains wetted upon impact.

*c. Internal cavity.* To further study the evolution characteristics of the internal cavity, Figs. 12 and 13 illustrate the internal cavity evolution in the vertical symmetry plane and a three-dimensional view of the hollow cylinder after closure, respectively.

The internal cavity is initially formed when the left cavity wall contacts the through-hole jet in Fig. 12(a). The left cavity is larger and fully wraps the left inner wall. However, the right inner wall is located in the backflow area and does not form a large enough cavity at the moment of impact. This wall remains wet after cavity closure. As the left cavity shrinks downward, passing through the cylinder tail, there is a brief period of contact between the fluid and the left tail. An impact force  $F_L$  is generated on the cylinder tail, producing a temporary clockwise moment relative to the mass center. This promotes the clockwise rotation of the hollow cylinder.

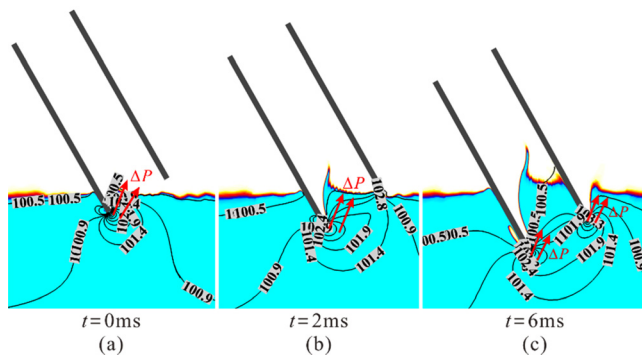


FIG. 11. Pressure contours (kPa) around the cylinder head from  $t = 0$ –6 ms.

As the cavity closure point moves to the right, the internal cavity separates from the atmosphere to form a closed cavity. The closed cavity is significantly compressed under the pressure of the surrounding fluid. The left internal cavity forms earlier and is squashed by the compression, as shown in Figs. 12(a)–12(c). Both contact points between the internal and external cavity and the cylinder wall move toward the cylinder head during the cavity contraction stage. The right internal cavity starts to form near the right inner head and gradually expands as the left internal cavity shrinks in Figs. 12(b)–12(e). This indicates that there is a formation sequence for the internal cavity in the case of oblique water entry, and the cavity in the backflow region appears relatively late. In addition, small shedding bubbles appear during the cavity contraction stage in Figs. 12(a) and 12(e) and backflow droplets are formed during the cavity expansion stage in Figs. 12(e) and 12(f).

During the initial formation of the internal cavity at  $t = 58$  ms, there is a gradual decrease in the internal cavity volume along the inner wall in Fig. 13(a). The left inner wall is fully wrapped by the left internal cavity, which has the largest size, while the right inner wall remains wet in the presence of the smaller right internal cavity. The front and rear inner walls are in an intermediate state between these two extremes. The internal cavity is mainly located to the lower-left of the inner hole, and its interface with the fluid is a diagonal line along a longitudinal section of the through-hole. As the left internal cavity shrinks and the cylinder rotates clockwise, the extruded internal air moves to the right along both the front and rear inner walls after cavity closure. This air pushes the surrounding fluid away from the wetted right inner wall and forms the right internal cavity. In summary, during the early stages, the left internal cavity shrinks while the right one expands, as shown in Figs. 13(a)–13(e). The internal air then oscillates to the right and left, resulting in a balanced cavity size on both sides in Fig. 13(f).

## 2. Motion hydrodynamics

*a. Movements of the hollow cylinder.* To investigate the transient motion of the hollow cylinder during oblique water entry, Fig. 14

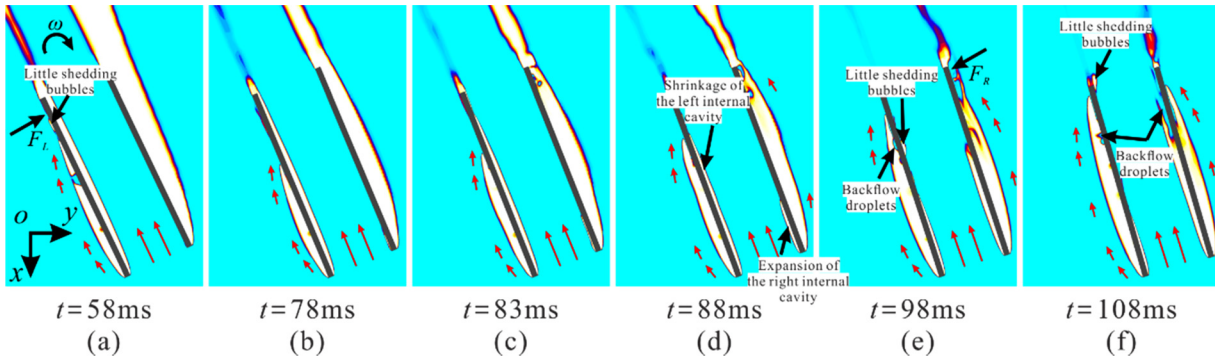


FIG. 12. Formation and evolution of the internal cavity in the oxy plane.

shows the variations in the trajectory of the head center, the projectile velocity  $v$ , and the vertical and horizontal components of velocity and acceleration with respect to time.

After water entry, the trajectory of the head center of the hollow cylinder follows a straight line until cavity closure in Fig. 14(a). The trajectory bends to the lower-left and becomes approximately parabolic. As shown in Fig. 14(b), the projectile velocity increases rapidly before impact ( $t < 0$  ms), but its growth is slowed by the fluid resistance upon water entry. The total velocity continues to increase with some small fluctuations, during the immersion process. This indicates that the acceleration effect of gravity on the cylinder is dominant under this operating condition.

According to Figs. 14(c) and 14(d), not all velocity components continue to increase, despite the steady growth in the total velocity of the projectile. In the horizontal direction, only fluid resistance acts on the projectile so the horizontal velocity  $v_x$  exhibits negative acceleration after water entry. Both fluid resistance and gravity act in the vertical direction, with the latter being dominant. The projectile acceleration decreases from  $g = 9.81 \text{ m/s}^2$  to about  $a_x = 3.7 \text{ m/s}^2$  with the flow resistance. Thus, the acceleration remains positive and  $v_x$  continues to increase. Furthermore, both  $v_x$  and  $v_y$  change in an almost linear fashion in Fig. 14(c). This indicates that the vertical and horizontal hydrodynamics force on the projectile are relatively stable during this period. The steady variation of velocity is interrupted after cavity closure.

The horizontal acceleration  $a_y$  and vertical acceleration  $a_x$  increase sharply soon after cavity closure in Fig. 14(d), leading to velocity fluctuations. As seen from the cavity evolution in Fig. 12(a), the left cavity shrinks downward and makes the left cylinder tail wet

upon cavity closure at  $t = 58$  ms. This short period in which the fluid and the left tail connect produces a certain impact force  $F_L$ , which pushes the cylinder in the horizontal direction. Thus,  $a_y$  increases sharply for a short time. However, this wet tail increases the fluid resistance in the vertical direction, causing  $a_x$  to decrease sharply and producing velocity fluctuations. As the closure point moves to the right form  $t = 88\text{--}98$  ms in Fig. 12(f), the right cavity shrinks and touches the rotated cylinder. This produces a reverse resistance force  $F_R$  in the horizontal direction, causing  $a_y$  to decrease sharply again. The left cavity gradually expands after the shrinkage and wraps around the cylinder, leading to the recovery of the vertical acceleration  $a_x$ . Thus, the tail-slap motion of the cylinder appears after water entry under this repeated fluid force from both sides. The acceleration oscillates multiple times in the latter stages, leading to velocity fluctuations. Overall, the horizontal velocity  $v_y$  tends to decrease and  $v_x$  tends to increase. However, the growth in  $v_x$  slows down with increasing water depth.

Figure 15 shows the variations in the pitch angle  $\theta_w$  of the hollow cylinder from  $t = 0\text{--}280$  ms. Here,  $\theta_w$  is defined as the angle between the cylinder central axis and the water surface, and effectively reflects the cylinder rotation after oblique water entry. As shown in Fig. 15, the initial value of  $\theta_w = 60^\circ$  is equal to the water-entry angle  $\alpha_w$  at the moment of impact. Thereafter,  $\theta_w$  increases in an approximately linear fashion before cavity closure. This indicates that the cylinder rotates clockwise at a relatively constant angular rate during this relatively stable stage. After cavity closure, the left cylinder tail touches the fluid first and generates a specific impact force. This induces a clockwise moment on the cylinder and causes  $\theta_w$  to increase rapidly for a short period at  $t > 58$  ms. The increasing trend then slows as the right

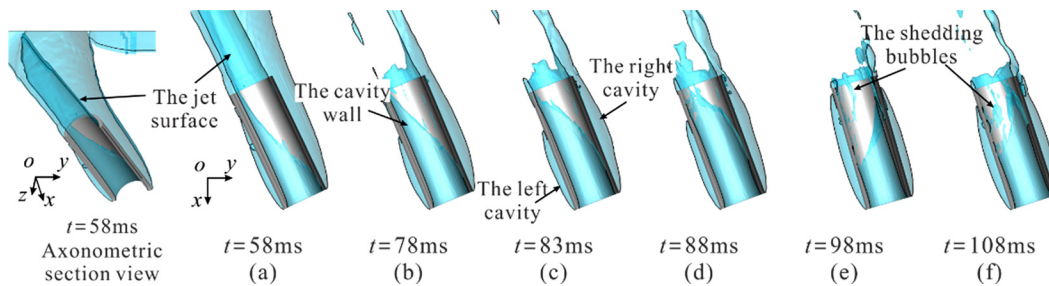


FIG. 13. Internal cavity evolution along the circumferential inner wall.

20 August 2024 01:09:19

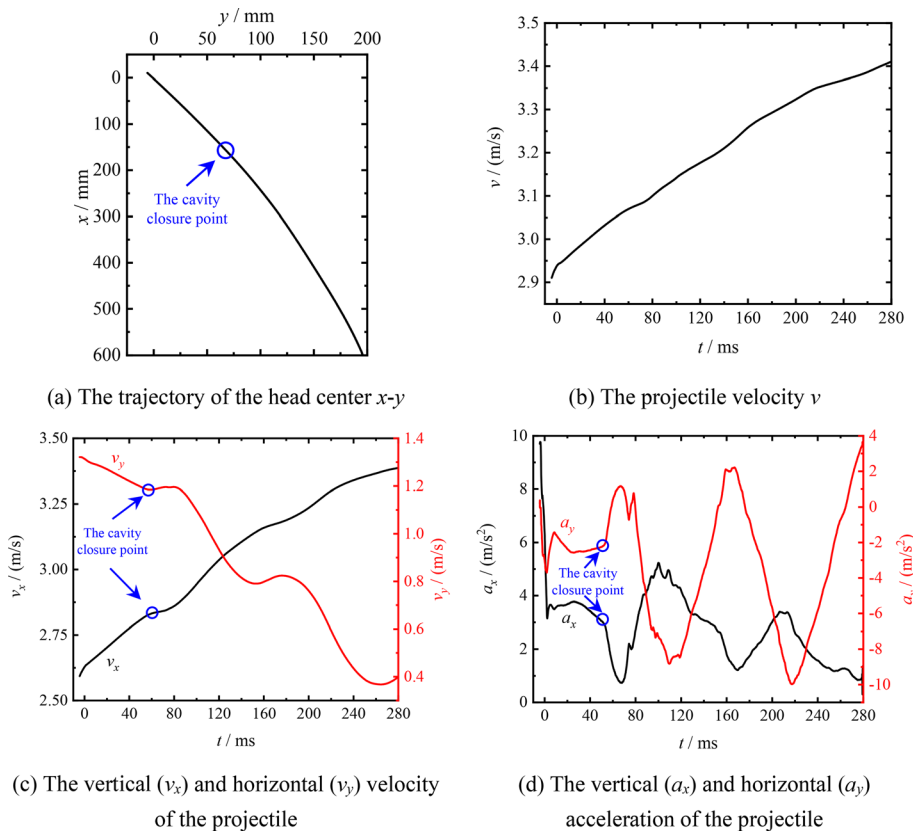


FIG. 14. Variations in motion parameters of the hollow cylinder from  $t=0-280$  ms ( $v_0 = 2.93$  m/s).

cylinder tail contacts the fluid, whereupon  $\theta_w$  experiences a short decrease under a reverse moment. In the latter stages, the pitch angle continues to increase and oscillates periodically with the cylinder motion. The periodic moment generated by the lateral fluid impact on both sides of the cylinder lasts for a long time. This induces the tail

slapping and left and right swings of the cylinder during the overall clockwise rotation.

*b. Hydrodynamic forces on the hollow cylinder.* To study the hydrodynamic forces on the hollow cylinder at various entry angles, the variations in flow resistance and moment during oblique water entry are shown in Figs. 16 and 17, respectively. Figure 16 shows the variations in the vertical ( $Drag_x$ ) and horizontal ( $Drag_y$ ) flow resistance on the cylinder during water entry. The resistance in both directions increases sharply upon impact with the water at  $t=0$  ms. Subsequently, the resistance fluctuates slightly and gradually stabilizes in the open cavity stage ( $t=0-50$  ms). Small changes in flow resistance occur during this stage, with a slowly increasing  $Drag_x$  and a slowly decreasing  $Drag_y$ . In the cavity closure stage ( $t=50-80$  ms), however,  $Drag_x$  increases sharply as the wetted area on the left cylinder tail is enhanced by the left cavity shrinkage. This fluid contact with the left cylinder tail produces a horizontal rightward impulsive force that results in a rapid decrease in  $Drag_y$ . This process explains the corresponding appearance of an acceleration saltation at the cavity closure point in Fig. 14(d), causing fluctuations in cylinder velocity.

As the cavity closure point moves to the right, the right cavity closure at  $t=80$  ms produces a reverse force, generating a sharp increase in  $Drag_y$ . The next cavity expansion decreases the wetted area of the cylinder and causes  $Drag_x$  to decrease sharply. In the latter tail-slap stage, the left and right cylinder tails touch the fluid periodically as the cavity volume oscillates. The corresponding fluid resistance varies

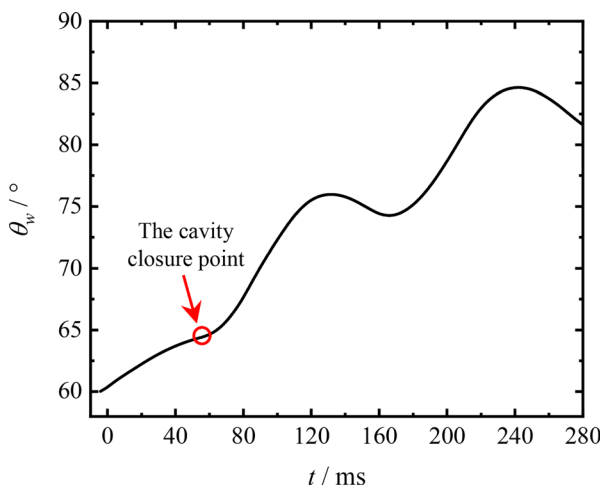


FIG. 15. Variations in pitch angle  $\theta_w$  of the hollow cylinder at  $\alpha_w = 60^\circ$ .

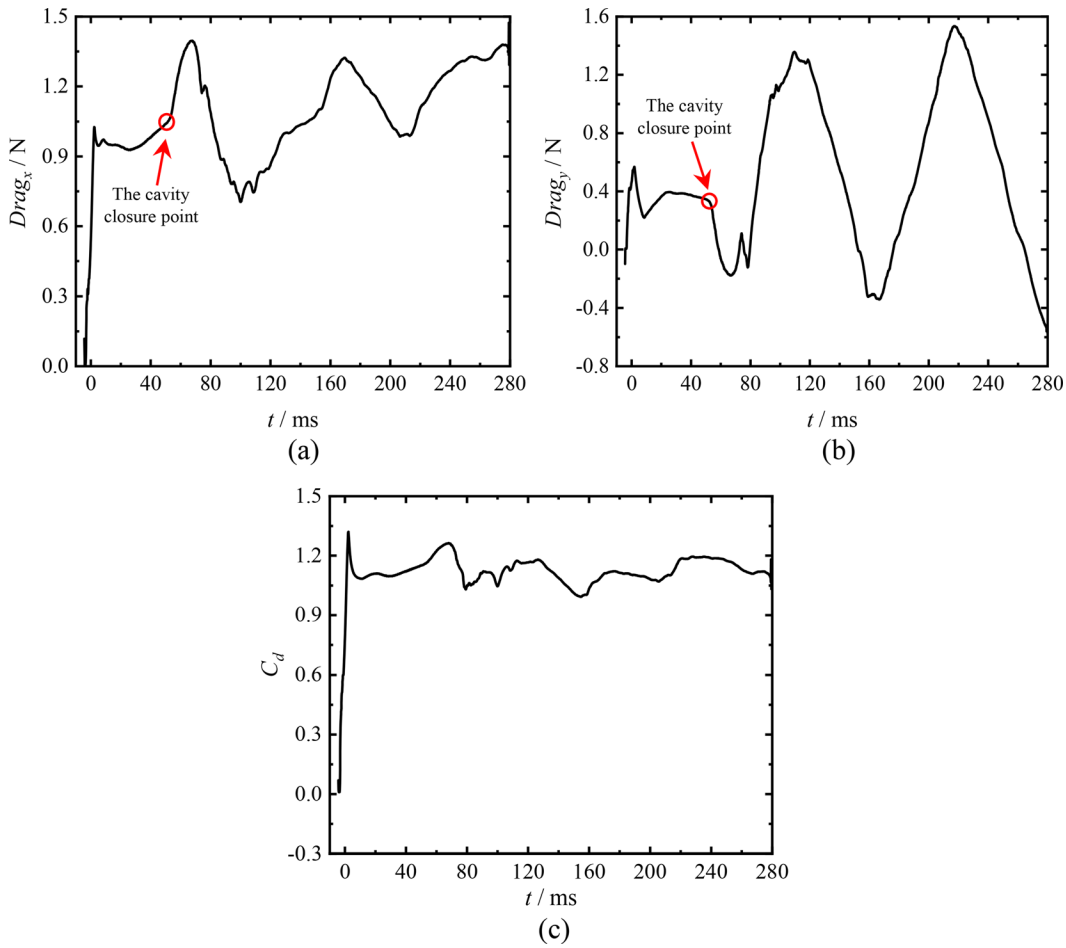


FIG. 16. Variations in (a) vertical resistance, (b) horizontal resistance and (c) resistance coefficient during oblique water entry at  $\alpha_w = 60^\circ$  and  $v_0 = 2.93$  m/s.

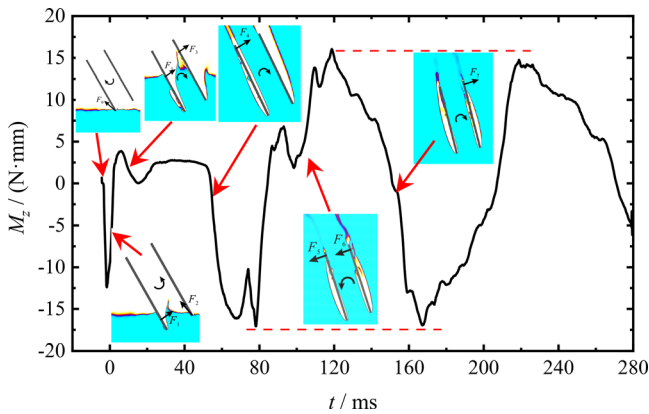


FIG. 17. Variations in the moment relative to the z-axis and forces exerted on the hollow cylinder at specific instants.

periodically, as shown in Fig. 16. Overall, the amplitude of  $Drag_x$  decreases significantly and tends to stabilize over time, but the amplitude of  $Drag_y$  gradually increases. This indicates that the motion instability of the cylinder is more significant in the horizontal direction.

Figure 17 shows the variations in the z-axis moment  $M_z$  exerted on the hollow cylinder as it enters the water at an angle. As the positive z-axis is defined as perpendicular to the vertical plane and pointing forward,  $M_z < 0$  represents a clockwise moment. To further analyze the mechanism of the moment variations, the flow forces exerted on the cylinder at specific instants are also shown.

The left side of the cylinder head hits the water surface first and induces the high pressure mainly in the left incident flow region. The fluid force ( $F_0$ ) acting on the head points to the upper-left and produces a clockwise moment relative to the mass center for a short time. Thus,  $M_z$  decrease sharply from  $t = -3$ – $0$  ms. Soon after, an impact force ( $F_1$ ) is generated by the right head hitting the water, and the fluid force becomes stronger as the wetted area of the left side in the

backflow region increases. These forces produce an anticlockwise moment on the cylinder for a short time, causing  $M_z$  to increase rapidly from  $t = 2-6$  ms. As the wetted part gradually spreads to the left tail with the formation of the left external cavity, the left fluid force begins to act on the left rear, and the internal splash rolls to the right and hits the bottom of the right inner wall. This provides a clockwise moment to the cylinder. Therefore,  $M_z$  experiences a slight decrease from  $t = 8-20$  ms before gradually stabilizing. In the latter period of the open cavity stage ( $t = 20-50$  ms), only the head and the right inner wall of the cylinder are wetted. The force acting on the cylinder is relatively stable and there is little change in the wetted area. Hence,  $M_z$  remains approximately unchanged until cavity closure at  $t = 58$  ms (Fig. 17).

The cavity closure generates a large fluctuation in  $M_z$ . A clockwise moment is first induced by the early collision ( $F_4$ ) between the left cavity and cylinder tail. This leads to a sharp decrease in  $M_z$  until the right cavity closure from  $t = 80-120$  ms. During this period, the external fluid hits the right outer tail and the internal jet hits the left inner tail due to the clockwise rotation of the cylinder. These impacts both produce a force to the left on the cylinder bottom and provide an anticlockwise moment to the cylinder. Therefore,  $M_z$  gradually increases. In the latter stages,  $M_z$  varies periodically with the alternate impact of the fluid on the left and right sides of the inner and outer tail. This causes the cylinder to sway left and right during water entry, and results in tail-slap motion. Furthermore, the amplitude of  $M_z$  is largely unchanged for a period in the latter stages ( $t = 60-280$  ms), with peaks and valleys of approximately 15 and  $-17$ , respectively. This indicates that the hollow cylinder swings steadily for a period of time after oblique water entry.

### C. Effects of entry angle

We now elucidate the effects of the entry angle on the cavity and motion characteristics during the oblique water entry of the hollow cylinder. This section presents the results of numerical simulations with entry angles of  $\alpha_w = 30^\circ-90^\circ$  at an entry speed of about  $v_0 = 3.09$  m/s with  $Fr = 7.8$ .

#### 1. External cavity

The cavity evolutions at entry angles of  $\alpha_w = 30^\circ, 45^\circ$ , and  $75^\circ$  are selected as examples to illustrate the typical characteristics of cavity

formation with the cylinder motion. Figures 18–20 show the external cavity evolution with these entry angles during oblique water entry.

When the entry angle is small ( $\alpha_w = 30^\circ$ , Fig. 18), the cavity asymmetry is evident, with a smaller cavity in the left backflow region and a larger cavity in the right incident flow region. The left open cavity barely wraps the left cylinder wall at  $t = 40$  ms. After its closure, the left cavity shrinks sharply under the high pressure of the fluid below, and the wetted area of the left outer wall of the cylinder gradually increases. With this small entry angle, the closure point of the left external cavity is located on the cylinder body and the classic deep closure only appears on the right external cavity. In the latter stages, the attached cavity is mainly located on the upper-right of the cylinder, and the cylinder exhibits significant anticlockwise rotation under the head-up moment induced by the upward force on the cylinder head.

When  $\alpha_w = 45^\circ$  in Fig. 19, the fundamental pattern of water-entry cavity evolution is similar to that when  $\alpha_w = 60^\circ$  in Figs. 8 and 9. The vertical velocity of the projectile increases as the entry angle rises from  $30^\circ$  to  $45^\circ$ . The left open cavity can fully wrap the entire cylinder as the cavity expands, and the closure point moves backward away from the cylinder tail. The left cavity closure occurs at  $t = 55$  ms, followed by the right cavity closure at  $t = 90$  ms. The shrinking left cavity hits the left cylinder tail, which produces a clockwise moment on the cylinder. The cylinder tends to rotate clockwise in the latter stages. The attached cavity swings left and right relative to the cylinder under the cylinder rotation, and the cavity size on both sides varies periodically. The left and right cylinder tails touch the outer fluid alternately, resulting in tail-slap motion.

The vertical entry velocity of the cylinder is further increased when  $\alpha_w$  rises to  $75^\circ$  in Fig. 20. The inside pressure of the cavity is lower and the splash convergence toward the center is accelerated by the pressure difference between the inside and outside cavities. Thus, the surface closure of the cavity around the water surface occurs at  $t = 40-55$  ms, and the closure point is located on the through-hole jet. The deep closure happens underwater after the cavity shrinkage. The water-entry angle causes these two closure patterns to begin asymmetrically from the left cavity closure on the through-hole jet. The closure point moves to the right, and the right cavity closure occurs at  $t = 75$  ms. The thin tail cavity that forms along the right closure point behind the right cavity is longer than that behind the left cavity. This

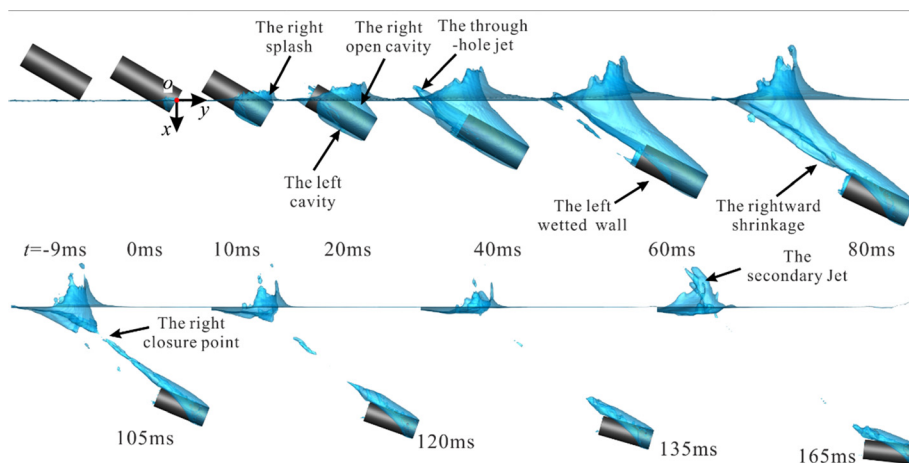


FIG. 18. Evolution of the external cavity during oblique water entry at  $\alpha_w = 30^\circ$ .

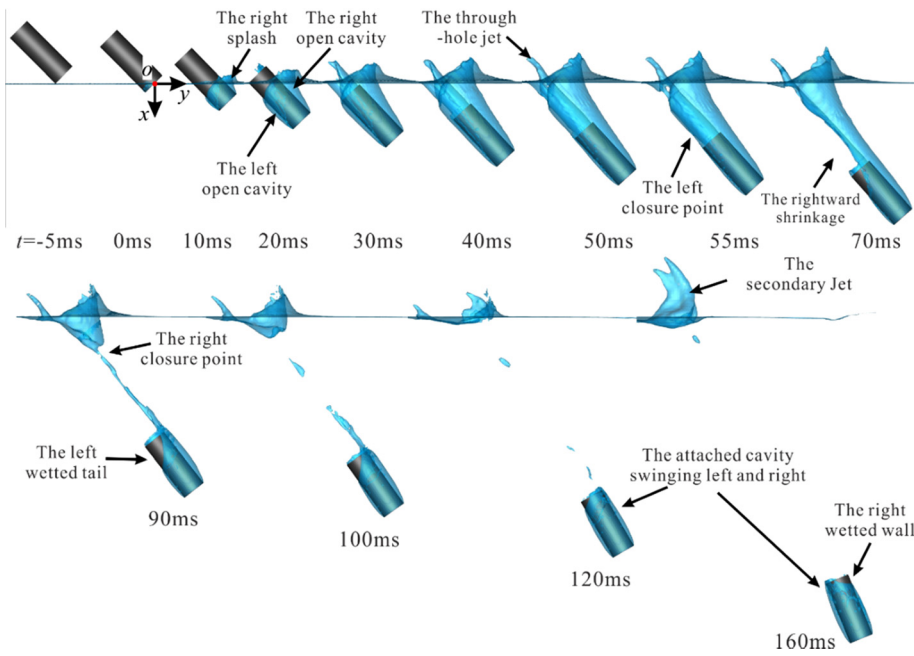


FIG. 19. Evolution of the external cavity during oblique water entry at  $\alpha_w = 45^\circ$ .

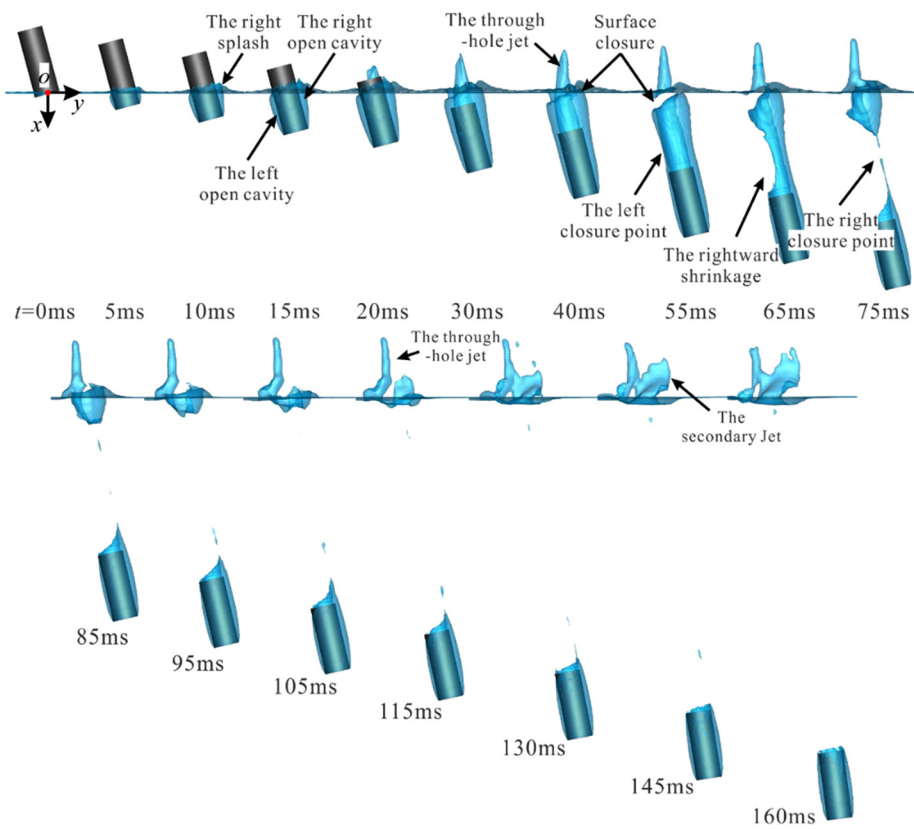


FIG. 20. Evolution of the external cavity during oblique water entry at  $\alpha_w = 75^\circ$ .

20 August 2024 01:09:19

tail cavity fades away with the shedding bubbles. Because the cavity closure point is far from the cylinder, no effective transient moment is produced by the impact between the fluid and the cylinder tail during the attached cavity formation. The attitude of the cylinder remains relatively stable.

**2. Through-hole jet and internal cavity**

Figure 21 shows the through-hole jet evolution at water-entry angles of  $\alpha_w = 30^\circ, 45^\circ,$  and  $75^\circ$ , illustrating their typical characteristics. When the water-entry angle is small [ $\alpha_w = 30^\circ$ , Fig. 21(a)], there is a longer entry distance between the water surface and the right head due to the inclined attitude. The internal rolling splash near the left inner wall reaches the right inner wall at  $t = 3$  ms, before the right head hits the water surface. The concave splash and the volume of the closed cavity on the right inner wall are relatively large at  $t = 6$  ms in the  $oxy$  plane. With the immersion of the right inner fluid, this closed cavity moves upward along the right inner wall and fades away after passing through the hole. The right side of the inner wall in the backflow area is always wet in this case. As  $\alpha_w$  increases to  $45^\circ$  [Fig. 21(b)], the water-entry distance of the right cylinder head decreases and the size of the concave splash is reduced. The left rolling splash does not

touch the right inner wall before exiting the hole ( $t = 15$  ms). However, the right side of the inner wall in the backflow area remains wet during the ascent stage of the through-hole jet.

When  $\alpha_w$  is further increased to  $75^\circ$  in Fig. 21(c), cavities are generated on both inner walls of the cylinder head after water-entry impact at  $t = 3$  ms. A concavity appears at the top of the jet and tends to form a top bubble. The through-hole jet evolution when  $\alpha_w = 75^\circ$  is similar to that in the vertical water-entry case. The differences between the backflow area and the incident flow area gradually decreases, but the through-hole jet still deviates to the right ( $t = 9$  ms). This is fundamentally due to the rolling internal splash to the right in the case of oblique water entry. In this case, the direction in which the through-hole jet is ejected deviates to the right ( $t = 30$  ms) after passing through the hole. To summarize the jet evolution characteristics in Fig. 21, the left inner wall hits the water first during oblique water entry, cutting the fluid apart near the water surface. The transmission of kinetic energy induces a rolling jet toward the upper-right inside the hole. If the internal jet tip passes through the hole without touching the right inner wall, the jet direction deviates to the right after exiting the hole. Decreasing the water-entry angle increases the tilt degree of the cylinder to the left and reduces the distance between the left and right inner walls. This makes it easier for the internal jet to touch the right inner

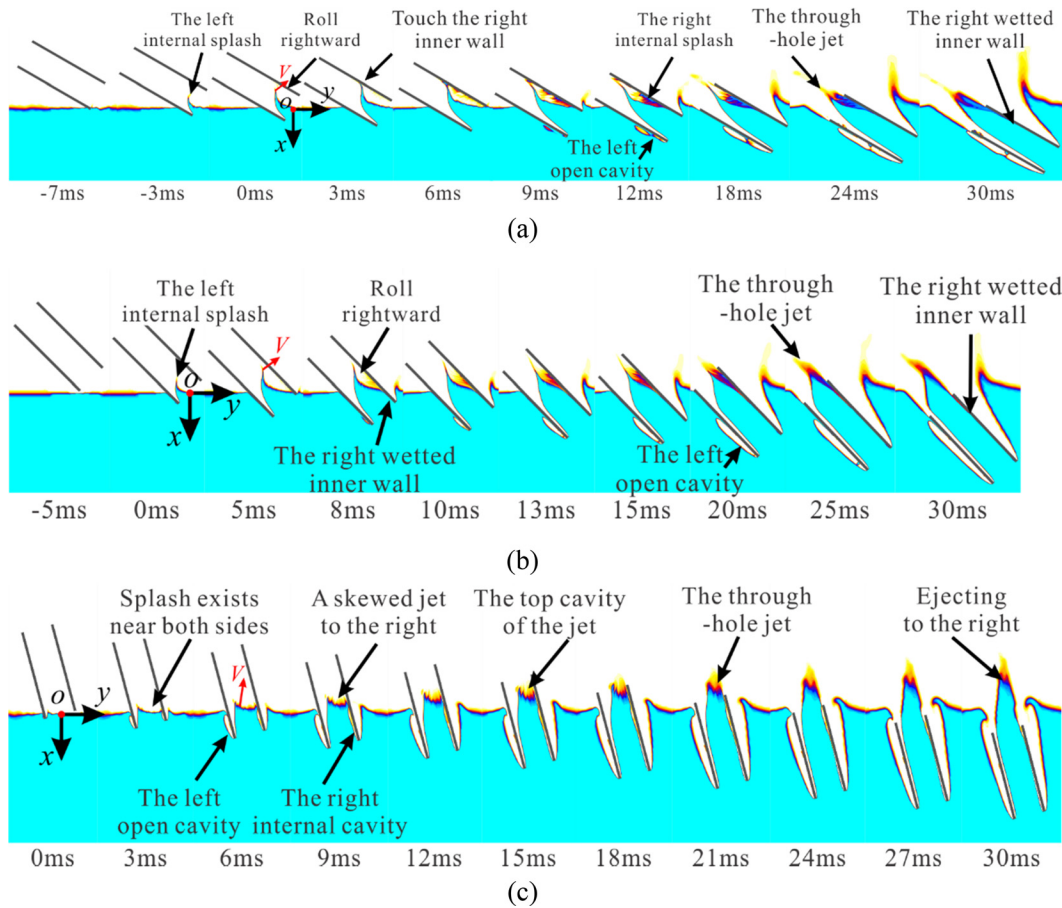


**FIG. 21.** Evolution of the through-hole jet at different water-entry angles in the  $oxy$  plane: (a)  $\alpha_w = 30^\circ$ , (b)  $\alpha_w = 45^\circ$  and (c)  $\alpha_w = 75^\circ$ .

20 August 2024 01:09:19

wall during the rising motion. The ejection direction is more strongly affected by the right inner wall, and gradually shifts in the opposite direction to the water entry of the cylinder. This explains the phenomenon of the altering jet direction in Fig. 21.

The internal cavity evolution at different water entry angles is shown in Fig. 22. When  $\alpha_w = 30^\circ$  in Fig. 22(a), the cylinder rotates anticlockwise with the right inner wall consistently wetted. The internal cavity only exists in the left incident flow region after the left cavity closure at  $t = 55$  ms. This internal cavity exhibits a gradual decrease in volume, and is finally located near the inner wall of the left cylinder tail. When  $\alpha_w = 45^\circ$  in Fig. 22(b), the right inner wall is still wetted and there are no internal cavities during the open cavity stage. However, a clockwise moment is induced on the cylinder by the impact between the left cavity and the cylinder tail after the left cavity closure. During the clockwise rotation of the cylinder, the left internal cavity swings to the right relative to the cylinder and forms the right internal cavity. In these two cases, the formation of the right internal

cavity depends on the direction of rotation (anticlockwise or clockwise) of the cylinder. When  $\alpha_w = 75^\circ$  in Fig. 22(c), the formation principle of the internal cavity is essentially similar to that in the case of vertical water entry. The fluid particles near the inner cylinder head move toward the cylinder axis under the high pressure induced by the impact. The separated flow forms internal cavities around both sides. The random interaction between the jet column and the inner wall under the Kelvin–Helmholtz instability determines the internal closure point. Similarly, the internal cavities are mainly located at the front of the inner wall ( $t = 130$  ms), with some random shedding bubbles. The cavity symmetry is enhanced in this case.

3. Motion characteristics

Figure 23 shows the variations in the motion parameters of the hollow cylinder during oblique water entry for  $\alpha_w = 30^\circ, 38^\circ, 45^\circ, 60^\circ,$  and  $75^\circ$ , including the trajectory, velocity, and acceleration of the

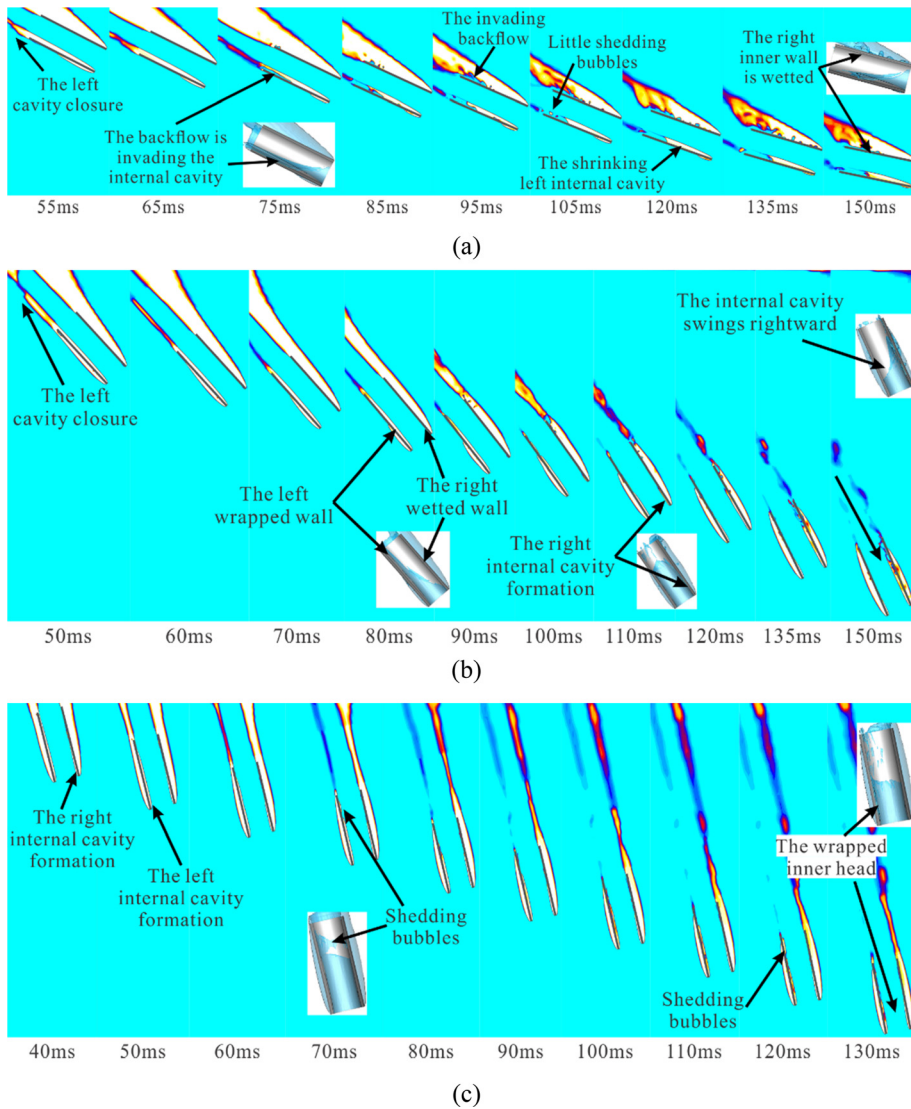
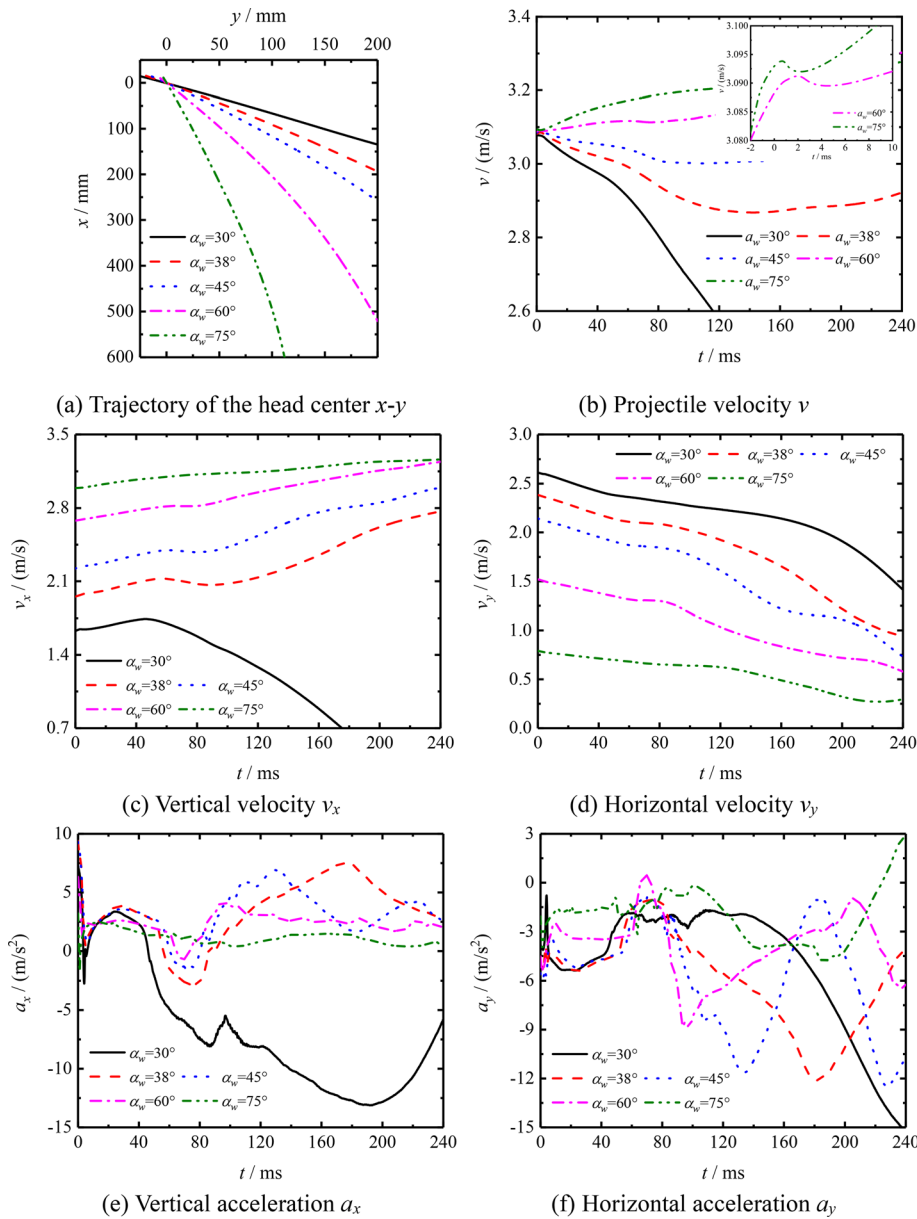


FIG. 22. Evolution of the internal cavity at different water-entry angles: (a)  $\alpha_w = 30^\circ$ , (b)  $\alpha_w = 45^\circ$  and (c)  $\alpha_w = 75^\circ$ .

20 August 2024 01:09:19





**FIG. 23.** Variations in motion parameters of the hollow cylinder at different entry angles.

cylinder. The motion trajectories of the head center are shown in Fig. 23(a). There is a clear deviation to the lower-left with increasing  $\alpha_w$  and a tendency to exhibit a parabolic shape. A significant clockwise deflection of the trajectory appears when  $\alpha_w \geq 45^\circ$  in the latter stages. Figures 23(b)–23(d) present the variations in the resultant velocity and velocity components of the cylinder. As seen from the resultant velocity of the cylinder after water entry, the overall variation trend of  $v$  shifts from downward ( $\alpha_w \leq 45^\circ$ ) to upward ( $\alpha_w > 45^\circ$ ) with increasing  $\alpha_w$  in Fig. 23(b). In fact, the cylinder  $v$  also decreases under the impact kinetic energy for the case of  $\alpha_w = 60^\circ$  and  $75^\circ$ , but it only happens within a short period ( $t = 0$ –6 ms) after the impact, as shown in the partial detail of Fig. 23(b).

After the impact, the projectile movement is primarily influenced by gravity and the fluid resistance. In the horizontal direction, the horizontal velocity  $v_y$  is mainly affected by the fluid resistance, so it continues to decrease continuously in Fig. 23(d). With the increase in  $\alpha_w$ , the initial  $v_y$  decreases with a less horizontal fluid resistance, which causes  $v_y$  to drop slowly. In the vertical direction, the vertical velocity  $v_x$  is affected by both the fluid resistance and gravity.

When  $\alpha_w = 30^\circ$ , the left bottom of the cylinder is clearly wetted at  $t > 40$  ms in Fig. 18. The vertical fluid resistance on the body rises significantly with the anticlockwise rotation of the cylinder and is greater than gravity. Thus,  $v_x$  exhibits a continuous decrease in Fig. 23(c). However, when  $\alpha_w > 45^\circ$ , the left cavity is enhanced and

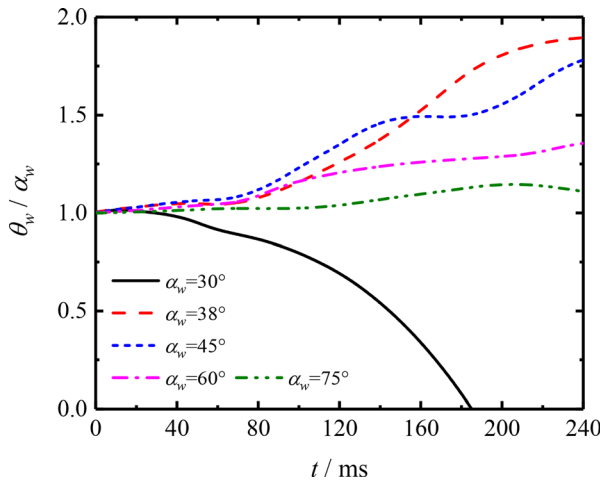


FIG. 24. Variations in pitch angle  $\theta_w$  of the hollow cylinder for various entry angles.

decreases the wetted area of the cylinder under the clockwise rotation. The vertical fluid resistance drops and is less than gravity. Thus, the vertical velocity  $v_x$  tends to increase under the dominant gravitational force. Especially for the cases of  $\alpha_w = 60^\circ$  and  $75^\circ$ , the vertical acceleration  $a_x$  is mostly positive in Fig. 23(e) and leads to the continuous increase in  $v_x$  in Fig. 23(c), which is more than the decrease rate of  $v_y$ . Therefore, the projectile velocity  $v$  obtained by vector calculation mainly increases after the impact in the case of  $\alpha_w = 60^\circ$  and  $75^\circ$ .

As shown in Figs. 23(e) and 23(f), an increase in  $\alpha_w$  mainly affects the cylinder acceleration after cavity closure ( $t > 80$  ms). In the case of  $\alpha_w = 30^\circ$ , the cylinder rotates anticlockwise with a small attached cavity. The vertical resistance is enhanced by the body rotation. Both  $a_x$  and  $a_y$  tend to decrease after cavity closure. When  $\alpha_w > 30^\circ$ , the cylinder mainly rotates clockwise and can be wrapped by more of the attached cavity. The fluid mostly touches the cylinder head during the immersion stage. Cavity closure produces a short flow impact on the cylinder tail and pushes the cylinder forward. Thus, in the vertical direction,  $a_x$  increases for some time after cavity closure. This rise time decreases as  $\alpha_w$  increases in Fig. 23(e). In the horizontal direction, the rotated cylinder alternately impacts the external fluid outside the cavity and the through-hole jet. A horizontal periodic force toward the left

and right is generated on the cylinder. Thus,  $a_y$  fluctuates after cavity closure in Fig. 23(f). When  $\alpha_w = 75^\circ$ , however, the cavity symmetry after cavity closure is enhanced and the situation is similar to that in the case of vertical water entry. Hence, the fluctuations in  $a_y$  are delayed by the weaker tail-slap motion of the cylinder body.

Figure 24 shows the variations in the pitch angle  $\theta_w$  of the hollow cylinder at different water-entry angles  $\alpha_w$ . A normalized value  $\theta_w / \alpha_w$  is defined to analyze the effects of changes in  $\alpha_w$ . When  $\alpha_w = 30^\circ$ , the cylinder only rotates anticlockwise and  $\theta_w$  decreases continuously. When  $\alpha_w > 30^\circ$ , the cylinder mainly rotates clockwise and  $\theta_w$  increases continuously. The cavity evolution becomes more symmetric as  $\alpha_w$  increases, and the rise amplitude of  $\theta_w$  relative to  $\alpha_w$  gradually decreases. This indicates that increasing  $\alpha_w$  weakens the rotational trend of the cylinder.

#### 4. Hydrodynamic force

The vertical and horizontal fluid resistance and the resistance coefficient of the hollow cylinder for various water-entry angles are shown in Figs. 25 and 26, respectively. As shown in Fig. 25, during the impact and open cavity stage ( $t < 50$  ms), the variations in the resistance are basically the same for all values of  $\alpha_w$ . The resistance increases sharply upon water-entry impact near  $t = 0$  ms, and then gradually recovers. After this initial fluctuation in Fig. 25(a),  $Drag_x$  rises again as the wetted portion of the cylinder increases. The rise amplitude depends on the size of the left wetted area. The left wetted area is reduced by the larger open cavity at higher  $\alpha_w$ , so the rise amplitude of  $Drag_x$  decreases accordingly. Regarding the horizontal resistance  $Drag_y$  in Fig. 25(b), the horizontal velocity of the cylinder decreases with increasing  $\alpha_w$  and generates horizontal fluid resistance. Hence, the rise amplitude of  $Drag_y$  also decreases.

In the latter stages ( $t = 80\text{--}200$  ms), the resistance tendency exhibits various characteristics as the direction of the cylinder changes. In the case of  $\alpha_w = 30^\circ$ , the overall wetted area of the cylinder is enlarged by the cylinder's anticlockwise rotation. The attached cavity becomes smaller and is located on the upper-right side. Thus, both  $Drag_x$  and  $Drag_y$  rise significantly under the increased fluid contact. For  $\alpha_w \geq 38^\circ$ , the cylinder rotates clockwise with a larger attached cavity and alternately impacts the cavity wall. Both  $Drag_x$  and  $Drag_y$  exhibit significant fluctuations under the induced tail-slap motion. However, the asymmetry of the attached cavity and the rotational

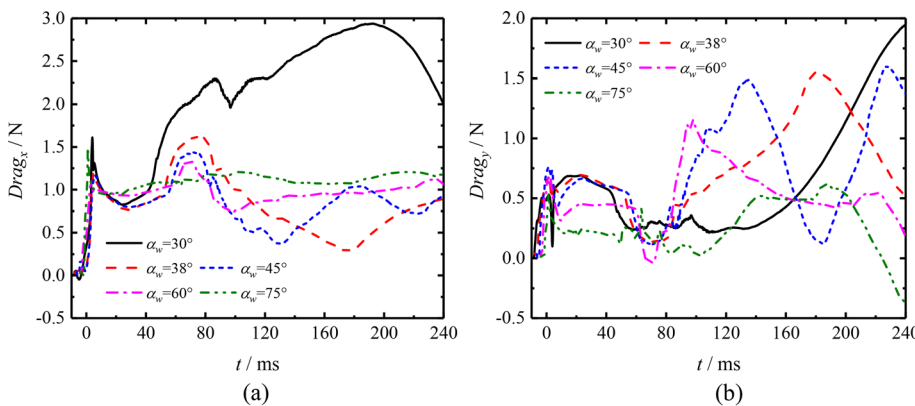


FIG. 25. Variations in (a) vertical and (b) horizontal flow resistance of the hollow cylinder at different entry angles.

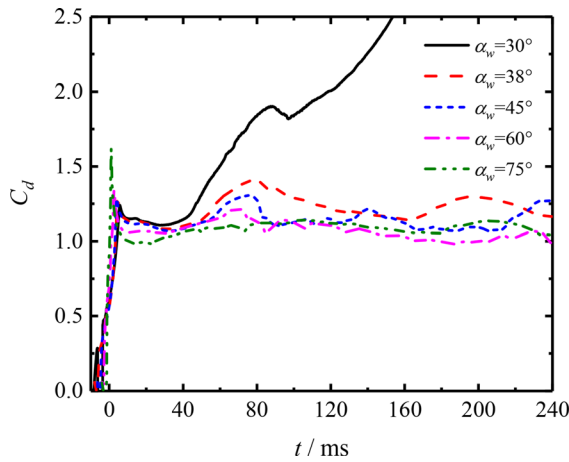


FIG. 26. Variations in the resistance coefficient  $C_d$  of the hollow cylinder at different entry angles.

trend of the cylinder decrease with increasing  $\alpha_w$ , so the fluctuations in resistance decrease.

For the resistance coefficient  $C_d$  in Fig. 26, an increase in  $\alpha_w$  enhances the peak value at the initial moment of impact. In the later stages, for  $\alpha_w = 30^\circ$ , the cylinder always rotates anticlockwise and its attitude finally becomes horizontal without motion stability. Thus,  $C_d$  continues to increase. When  $\alpha_w \geq 38^\circ$ , the cylinder mainly rotates clockwise and exhibits stable downward movement with a wrapped cavity. Hence,  $C_d$  fluctuates in the range of 1.0–1.5, and the fluctuation amplitude decreases with increasing  $\alpha_w$ . In summary, there is a critical entry angle for ensuring motion stability during the low-speed oblique water entry of the hollow cylinder. When  $\alpha_w$  is greater than this critical value, the cylinder rotates clockwise and moves downward stably after water entry. For the oblique water entry of the hollow cylinder considered in this paper, the critical water-entry angle  $\alpha_w$  is between  $30^\circ$  and  $38^\circ$  at  $v_0 = 3.09$  m/s.

The variations in the moment  $M_z$  on the hollow cylinder for various  $\alpha_w$  are shown in Fig. 27. The valley  $M_z$  near  $t = 0$  ms initially deepens with increasing  $\alpha_w$ , before becoming shallower when  $\alpha_w > 45^\circ$ .

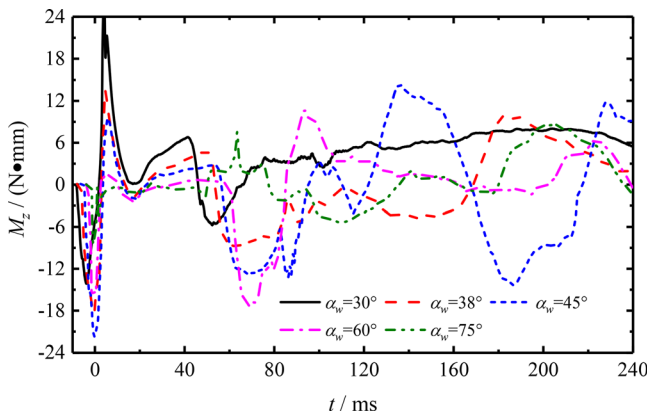


FIG. 27. Variations in the moment  $M_z$  of the hollow cylinder at different entry angles.

The shallowest valley occurs at  $\alpha_w = 45^\circ$ . This indicates that the largest clockwise moment induced by the initial impact between the left cylinder head and the water occurs when  $\alpha_w = 45^\circ$ . Similarly, the largest anticlockwise moment near  $t = 10$  ms occurs at  $\alpha_w = 30^\circ$ , when the right cylinder head hits the water. In the latter stages of the case  $\alpha_w = 30^\circ$ , the cylinder is mainly affected by the anticlockwise moment from the greater proportion of the body being wetted. The cylinder rotates anticlockwise during the entire process under a generally positive moment  $M_z$ . For  $\alpha_w \geq 38^\circ$ , the cylinder undergoes an initial clockwise moment upon entering the water, with an additional clockwise moment induced by the impact of the left cavity during the cavity closure stage. Therefore, the cylinder tends to rotate clockwise after immersion. The later fluctuations of  $M_z$  are mainly induced by the alternate impacts of the cylinder and fluid on both sides. The cylinder exhibits tail-slapping motion with a wrapped cavity during this process.

To clarify the extreme difference of  $C_d$  in the later stage between the case of  $\alpha_w = 30^\circ$  and  $\alpha_w \geq 38^\circ$  in Fig. 26, the comparison of cylinder attitude and cavity shape between the typical case of  $\alpha_w = 30^\circ$  and  $38^\circ$  is shown in Fig. 28. After the attitude adjustment caused by the impact and cavity closure, the cylinder will rotate in a steady direction. When  $\alpha_w \geq 38^\circ$ , the cylinder rotates clockwise in the later stage and the wet tail can enter the cavity again, as shown in Fig. 28. The cylinder moves downward with the body wrapped by the cavity finally. The wet area of cylinder varies periodically with tail-slap motion. Thus, the resistance coefficient  $C_d$  will fluctuate within a specific range in Fig. 26. However, when  $\alpha_w = 30^\circ$ , the cylinder rotates anticlockwise and moves away from the upper-right cavity gradually in Fig. 28. The wet area expands rapidly and the cylinder attitude tends to be horizontal, which enhance the fluid resistance. Therefore,  $C_d$  for the case of  $\alpha_w = 30^\circ$  increases sharply finally in Fig. 26.

To dig out the critical characteristics of the direction change, the cases of  $\alpha_w = 31, 32, 33,$  and  $35$  degrees are simulated and their hydrodynamic variations are shown in Figs. 29 and 30.

The attitude and flow resistance of the hollow cylinder at  $\alpha_w = 30^\circ - 38^\circ$  are shown in Fig. 29. In all cases, the cylinder undergoes three attitude adjustments during the early stage, rotating clockwise, then anticlockwise and finally clockwise again, as shown in the partial detail ( $t = 0 - 80$  ms) of Fig. 29(a). The clockwise rotation is weakened, and the anticlockwise rotation is enhanced with the decrease in  $\alpha_w$  from  $38^\circ$  to  $30^\circ$ . The critical condition occurs at  $\alpha_w = 32^\circ$  when the extreme point reaches but does not exceed 1 at about  $t = 125$  ms in the third adjustment. When  $\alpha_w \leq 32^\circ$ , the cylinder rotates anticlockwise in the

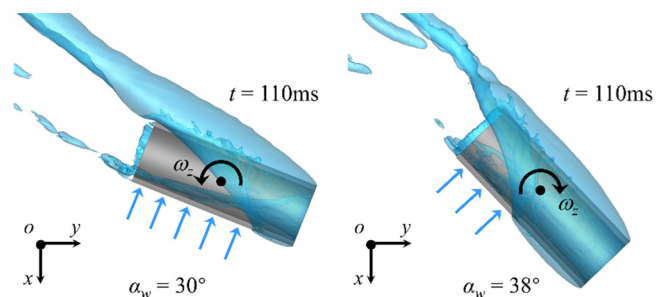


FIG. 28. The comparison of cylinder attitude and cavity shape between  $\alpha_w = 30^\circ$  and  $38^\circ$ .

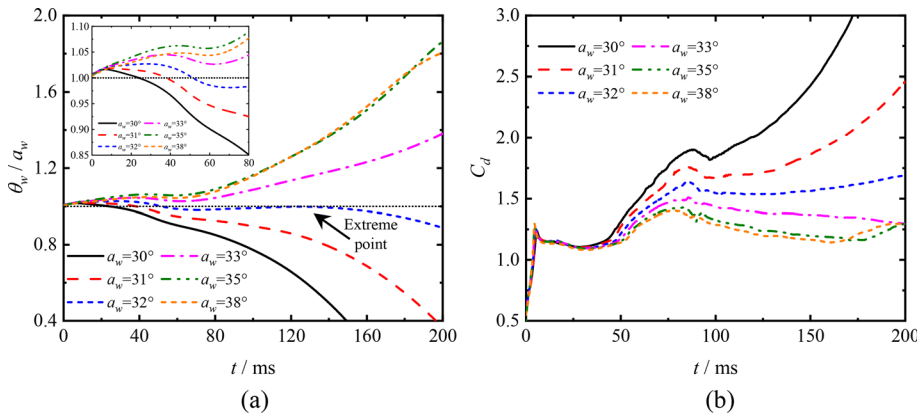


FIG. 29. Variations in (a) pitch angle  $\theta_w$  and (b) resistance coefficient  $C_d$  of the hollow cylinder at  $\alpha_w = 30^\circ\text{--}38^\circ$ .

later stage and this trend becomes more significant as  $\alpha_w$  decreases. As seen from Fig. 30, the moment  $M_z$  mainly fluctuates within  $-24\text{--}30$  N·mm and is almost positive at  $\alpha_w \leq 32^\circ$  with an inclined body axis. The anticlockwise moment  $M_z$  induced by the flow force and gravity is enhanced with the decreasing  $\alpha_w$ . Therefore, as  $\alpha_w$  decreases, the cylinder tends to rotate anticlockwise, leading to an accelerated growth rate of  $C_d$  in later stage in Fig. 29(b).

IV. CONCLUSIONS

This work investigates the oblique water entry of a hollow cylinder at different water-entry angles numerically. Our numerical results are in good agreement with corresponding experimental results. We have identified the disparities between vertical and oblique water entry of a hollow cylinder. The effects of changes in the water-entry angle on the cavity evolution and motion hydrodynamics are analyzed, including internal and external cavities, cylinder trajectory deflection, and attitude rotation. The main findings of this work are summarized as follows:

- (1) During the oblique water entry of a hollow cylinder, asymmetric attached cavities form near both the inner and outer walls. The external cavity in the backflow region near the left cylinder side is relatively small and the left deep closure occurs earlier. The left cylinder side undergoes wetting during both water entry

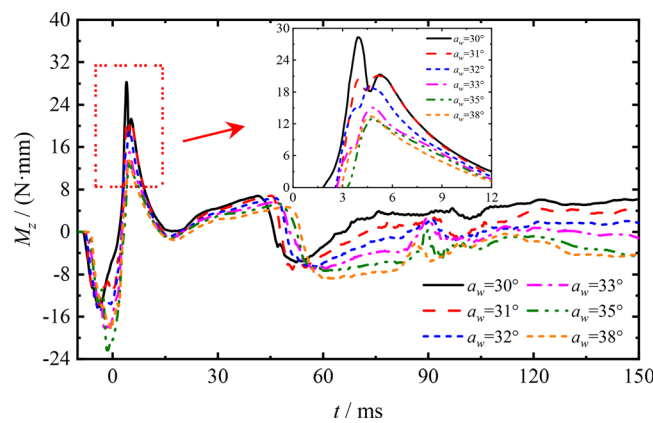


FIG. 30. Variations in the moment  $M_z$  of the hollow cylinder at  $\alpha_w = 30^\circ\text{--}38^\circ$ .

- and cavity closure. The left external cavity becomes larger and the wetted area decreases with increasing water-entry angle.
- (2) The left internal cavity is mainly formed by the cavity shrinkage inside the hole after cavity closure. The right inner cavity has different formation mechanisms depending on the water-entry angle. When the water-entry angle is large, the formation mechanism is the same as for the left cavity. However, the right inner wall is fully wetted in the early stages at small water-entry angle. Hence, the right internal cavity is formed by fluid separation when the left inner cavity shifts rightwards along the front and back inner walls.
- (3) An inward concavity forms on the through-hole jet tip under the rightward curling of the left internal splash. The left-curling splash touches the right inner wall and moves upward with the guidance of the inner wall. When the internal jet passes through the hole, its ejection direction changes from upper-left to upper-right with increasing water-entry angle. The initial impact can decelerate the cylinder within 0–5 ms, but gravity dominates and is greater than the fluid resistance and accelerates the cylinder in the later stage at water-entry angle of  $60^\circ$  and  $75^\circ$ . The resistance coefficient of hollow cylinder fluctuates in the range of 1.0–1.5 at  $\alpha_w \geq 38^\circ$ , but the anticlockwise rotation of cylinder increases the resistance coefficient sharply in the later period.
- (4) There is a critical water-entry angle classifying the direction of the hollow cylinder rotation, which is estimated to be  $32^\circ$ . The hollow cylinder is mostly subjected to positive moments and rotates counterclockwise at  $\alpha_w \leq 32^\circ$ . When above this critical angle, a significant clockwise moment is induced by the left high-pressure region on the inner head and the impact between the left cavity and cylinder tail, causing the clockwise rotation of cylinder after water entry. The cylinder tail and the inner wall alternately impact the external fluid and the internal jet during the clockwise rotation, resulting in a steady tail-slap motion under a periodic hydrodynamic force and moment.

ACKNOWLEDGMENTS

This work was supported by the National Natural Science Foundation of China (No. 12002165).

20 August 2024 01:09:19

## AUTHOR DECLARATIONS

## Conflict of Interest

The authors have no conflicts to disclose.

## Author Contributions

**Zhengui Huang:** Funding acquisition (lead); Resources (equal); Software (equal); Writing – review & editing (equal). **Yu Hou:** Conceptualization (lead); Formal analysis (equal); Investigation (lead); Writing – original draft (lead). **Xiaowei Cai:** Validation (equal). **Zhihua Chen:** Investigation (equal). **Yiming Xu:** Data curation (equal). **Jian Qin:** Software (equal).

## DATA AVAILABILITY

The data that support the findings of this study are available from the corresponding author upon reasonable request.

## REFERENCES

- <sup>1</sup>T. T. Truscott, B. P. Epps, and J. Belden, “Water entry of projectiles,” *Annu. Rev. Fluid Mech.* **46**, 355–378 (2014).
- <sup>2</sup>S. Xia, Y. Wei, C. Wang, W. Cao, and X. Hu, “Numerical investigation of the high-speed vertical water entry of a cylindrical shell,” *Phys. Fluids* **35**(3), 035132 (2023).
- <sup>3</sup>M. Jalalisendi and M. Porfiri, “Water entry of cylindrical shells: Theory and experiments,” *AIAA J.* **56**(11), 4500–4514 (2018).
- <sup>4</sup>R. Panciroli, S. Ubertini, G. Minak, and E. Jannelli, “Experiments on the dynamics of flexible cylindrical shells impacting on a water surface,” *Exp. Mech.* **55**(8), 1537–1550 (2015).
- <sup>5</sup>C. F. Babbs, “Stone skipping physics,” *Phys. Teach.* **57**(5), 278–281 (2019).
- <sup>6</sup>S. I. Sharker, S. Ubertini, M. M. Mansoor, F. E. Fish, and T. T. Truscott, “Water entry impact dynamics of diving birds,” *Bioinspir. Biomim.* **14**(5), 056013 (2019).
- <sup>7</sup>J. W. Glasheen and T. A. McMahon, “A hydrodynamic model of locomotion in the Basilisk Lizard,” *Nature* **380**(6572), 340–342 (1996).
- <sup>8</sup>T. Guillet, M. Mouchet, J. Belayachi, S. Fay, D. Colturi, P. Lundstam, P. Hosoi, C. Clanet, and C. Cohen, “The hydrodynamics of high diving,” in *73th Annual Meeting APS Division Fluid Dynamics* (MDPI, 2020), Vol. 49(1), pp. 1–6.
- <sup>9</sup>S. Feng, W. Mingzhen, Z. Jiaxu, and H. Qi, “Numerical simulation method for wave surface landing of seaplane,” *IOP Conf. Ser. Mater. Sci. Eng.* **751**(1), 012061 (2020).
- <sup>10</sup>H. Zeraatgar, J. Malekmohammadi, M. J. Javaherian, and H. Moradi, “Sampling rate effect on wedge pressure record in water entry by experiment,” *Ocean Eng.* **179**, 51–58 (2019).
- <sup>11</sup>Y. Shi, G. Wang, and G. Pan, “Experimental study on cavity dynamics of projectile water entry with different physical parameters,” *Phys. Fluids* **31**(6), 067103 (2019).
- <sup>12</sup>C. Wang, Q. Huang, L. Lu, G. Pan, and S. Gao, “Numerical investigation of water entry characteristics of a projectile in the wave environment,” *Ocean Eng.* **294**, 116821 (2024).
- <sup>13</sup>T. T. Truscott, J. T. Gomez, D. N. Beal, and A. H. Techet, “Shallow angle water entry of ballistic projectiles,” in *7th International Symposium on Cavitation* (ASME, Ann Arbor, Michigan, 2009).
- <sup>14</sup>T. T. Truscott, B. P. Epps, and A. H. Techet, “Unsteady forces on spheres during free-surface water entry,” *J. Fluid Mech.* **704**, 173–210 (2012).
- <sup>15</sup>J. M. Aristoff, T. T. Truscott, A. H. Techet, and J. W. M. Bush, “The water entry of decelerating spheres,” *Phys. Fluids* **22**(3), 032102 (2010).
- <sup>16</sup>N. Kim and H. Park, “Water entry of rounded cylindrical bodies with different aspect ratios and surface conditions,” *J. Fluid Mech.* **863**, 757–788 (2019).
- <sup>17</sup>A. H. Techet and T. T. Truscott, “Water entry of spinning hydrophobic and hydrophilic spheres,” *J. Fluids Struct.* **27**(5–6), 716–726 (2011).
- <sup>18</sup>J. M. Aristoff and J. W. M. Bush, “Water entry of small hydrophobic spheres,” *J. Fluid Mech.* **619**, 45–78 (2009).
- <sup>19</sup>T. T. Truscott and A. H. Techet, “Water entry of spinning spheres,” *J. Fluid Mech.* **625**, 135–165 (2009).
- <sup>20</sup>X. J. Lyu, X. Wang, C. Qi, and R. S. Sun, “Characteristics of cavity dynamics, forces, and trajectories on vertical water entries with two spheres side-by-side,” *Phys. Fluids* **35**(9), 092101 (2023).
- <sup>21</sup>X. J. Lyu, H. L. Yun, and Z. Y. Wei, “Influence of time interval on the water entry of two spheres in tandem configuration,” *Exp. Fluids* **62**(11), 222 (2021).
- <sup>22</sup>S. Gekle, I. R. Peters, J. M. Gordillo, D. van der Meer, and D. Lohse, “Supersonic air flow due to solid-liquid impact,” *Phys. Rev. Lett.* **104**(2), 024501 (2010).
- <sup>23</sup>R. Bergmann, D. van der Meer, S. Gekle, A. van der Bos, and D. Lohse, “Controlled impact of a disk on a water surface: Cavity dynamics,” *J. Fluid Mech.* **633**, 381–409 (2009).
- <sup>24</sup>J.-F. Louf, B. Chang, J. Eshraghi, A. Mituniewicz, P. P. Vlachos, and S. Jung, “Cavity ripple dynamics after pinch-off,” *J. Fluid Mech.* **850**, 611–623 (2018).
- <sup>25</sup>G. X. Yan, G. Pan, Y. Shi, and G. H. Wang, “Experimental study on water entry of cylindrical projectiles with different nose shapes,” *Mod. Phys. Lett. B* **33**(9), 1950107 (2019).
- <sup>26</sup>T. Chen, W. Huang, W. Zhang, Y. F. Qi, and Z. T. Guo, “Experimental investigation on trajectory stability of high-speed water entry projectiles,” *Ocean Eng.* **175**, 16–24 (2019).
- <sup>27</sup>L. Yi, S. Li, H. C. Jiang, D. Lohse, C. Sun, and V. Mathai, “Water entry of spheres into a rotating liquid,” *J. Fluid Mech.* **912**, R1–10 (2021).
- <sup>28</sup>C. Qi, X. Lyu, X. Wang, H. Ye, H. Shi, and Z. Wan, “Experimental and numerical studies on vertical water entry of a cylinder under the influence of current,” *Phys. Fluids* **36**(3), 033322 (2024).
- <sup>29</sup>X. Hu, Y. Wei, and C. Wang, “Effect of fluid–structure interaction on the oblique water entry of the projectile under the influence of floating ice structure,” *Phys. Fluids* **36**(4), 043331 (2024).
- <sup>30</sup>H. Wang, Z. G. Huang, D. Huang, Y. Hou, Z. H. Chen, Z. Q. Guo, S. Sun, and R. Y. X. Xue, “Influences of floating ice on the vertical water entry process of a trans-media projectile at high speeds,” *Ocean Eng.* **265**, 112548 (2022).
- <sup>31</sup>W. Li, C. Wang, Y. Wei, S. Xia, and Y. Ding, “Experimental study on vertical water entry of the projectile with canard-wing,” *Phys. Fluids* **36**(3), 033356 (2024).
- <sup>32</sup>Q. Z. Yang, F. Xu, Y. Yang, J. Y. Wang, A. W. Wang, and C. H. Ma, “Numerical study on the dynamic characteristics of water entry of cavity body using two-phase SPH method,” *Acta Mech. Sin.* **37**(7), 1072–1089 (2021).
- <sup>33</sup>H. Liu, J. T. Pi, B. Zhou, L. Chen, Q. Fu, and G. Y. Zhang, “Experimental investigation on the multiphase flow characteristics of oblique water entry of semi-closed cylinder,” *Ocean Eng.* **239**, 109819 (2021).
- <sup>34</sup>M.-A. Jafari and P. Akbarzadeh, “Experimental analysis of water entry problem considering hollow cylinders: The impact of hole geometry,” *Ocean Eng.* **259**, 111906 (2022).
- <sup>35</sup>Y. Hou, Z. Huang, Z. Chen, Z. Guo, and Y. Xu, “Experimental investigations on the oblique water entry of hollow cylinders,” *Ocean Eng.* **266**, 112800 (2022).
- <sup>36</sup>B. Zhou, H. Liu, Y. Wang, Z. Wu, X. Han, and W. M. Gho, “Numerical investigation on the cavity dynamics and multiphase flow field evolution for water entry of vertical cylindrical shell,” *J. Fluids Struct.* **103**, 103268 (2021).
- <sup>37</sup>X. Y. Zhang, Y. Shi, G. Pan, and Q. G. Huang, “Study on the impact performance of sandwich hollow cylinders hitting water based on SPH method,” *Ocean Eng.* **197**, 106808 (2020).
- <sup>38</sup>Y. Hou, Z. Huang, Z. Chen, Z. Guo, and Y. Luo, “Investigations on the vertical water-entry of a hollow cylinder with deep-closure pattern,” *Ocean Eng.* **190**, 106426 (2019).
- <sup>39</sup>H. Shokri and P. Akbarzadeh, “Experimental investigation of water entry of dimpled spheres,” *Ocean Eng.* **250**, 110992 (2022).
- <sup>40</sup>H. Sun and O. M. Faltinsen, “Water impact of horizontal circular cylinders and cylindrical shells,” *Appl. Ocean Res.* **28**(5), 299–311 (2006).
- <sup>41</sup>X. Lyu, Z. Wei, H. Tang, T. H. New, and H. Li, “On the motion of a falling circular cylinder in flows after water entry,” in *International Conference on Experimental Mechanics 2014* (SPIE, 2015).
- <sup>42</sup>M.-R. Erfanian and M. Anbarsooz, “Numerical investigation of body and hole effects on the cavitating flow behind a disk cavitator at extremely low cavitation numbers,” *Appl. Math. Modell.* **62**, 163–180 (2018).

- <sup>43</sup>Y. Hou, Z. Huang, Z. Chen, Z. Guo, and L. Han, "Different closure patterns of the hollow cylinder cavities with various water-entry velocities," *Ocean Eng.* **221**, 108526 (2021).
- <sup>44</sup>H. W. Fan, Z. G. Huang, H. Wang, Z. H. Chen, X. Y. Liu, F. J. Xiao, and R. X. Qiu, "Numerical study of high-speed vertical water entry of hollow projectiles with different aperture sizes and velocities," *J. Appl. Fluid Mech.* **16**(11), 2219–2234 (2023).
- <sup>45</sup>G. Y. Zhang, Z. Hou, T. Z. Sun, H. P. Wei, N. Li, B. Zhou, and Y. J. Gao, "Numerical simulation of the effect of waves on cavity dynamics for oblique water entry of a cylinder," *J. Hydrodyn.* **32**(6), 1178–1190 (2020).
- <sup>46</sup>H. Liu, B. Zhou, J. Yu, K. Liu, X. Han, and G. Zhang, "Experimental investigation on the multiphase flow characteristics of oblique water entry of the hollow cylinders," *Ocean Eng.* **272**, 113902 (2023).
- <sup>47</sup>T. H. Shih, W. W. Liou, A. Shabbir, Z. Yang, and J. Zhu, "A new k- $\epsilon$  eddy viscosity model for high Reynolds number turbulent flows," *Comput. Fluids* **24**(3), 227–238 (1995).